Development of a ReaxFF reactive force field for lithium ion conducting solid electrolyte $Li_{1+x}Al_xTi_{2-x}(PO_4)_3$ (LATP)

Journal:	*Physical Chemistry Chemical Physics*
Manuscript ID	CP-ART-06-2018-003586.R1
Article Type:	Paper
Date Submitted by the Author:	20-Jul-2018
Complete List of Authors:	Shin, Yun Kyung; Pennsylvania State University, Mechanical and Nuclear Engineering Sengul, Mert; Pennsylvania State University Jonayat, ASM; Pennsylvania State University, Mechanical and Nuclear Engineering Lee, Wonho; The Pennsylvania State University Gomez, Enrique; The Pennsylvania State University Randall, Clive; Pennsylvania State University, Center for Dielectric Studies, Materials Research Institute, University Park, Pa 16802 USA, Duin, Adri ; The Pennsylvania State University

SCHOLARONE™
Manuscripts

Development of a ReaxFF reactive force field for lithium ion conducting solid electrolyte $Li_{1+x}Al_xTi_{2-x}(PO_4)_3$ (LATP)

Yun Kyung Shin,[†] Mert Y. Sengul,[†,‖] A. S. M. Jonayat,[†] Wonho Lee,[‡] Enrique D. Gomez,[‡,‖] Clive A. Randall[‖] and Adri C. T. van Duin*,[†]

[†] Department of Mechanical and Nuclear Engineering, Pennsylvania State University, University Park, Pennsylvania 16802, United States

[‡] Department of Chemical Engineering, Pennsylvania State University, University Park, Pennsylvania 16802, United States

[‖] Department of Materials Science and Engineering, Materials Research Institute, Pennsylvania State University, University Park, Pennsylvania 16802, United States

* Corresponding author: acv13@engr.psu.edu

Abstract We developed a ReaxFF reactive force field for NASICON-type $Li_{1+x}Al_xTi_{2-x}(PO_4)_3$ (LATP) materials, which is a promising solid-electrolyte that may enable all-solid-state lithium-ion batteries. The force field parameters were optimized based on density functional theory (DFT) data, including equations of state and the heats of formation of ternary metal oxides and metal phosphates crystal phases (e.g., Li_xTiO_2, Al_2TiO_5, $LiAlO_2$, $AlPO_4$, Li_3PO_4 and $LiTi_2(PO_4)_3$ (LTP)), and the energy barriers for Li diffusion in TiO_2 and LTP via vacancies and interstitial sites. Using ReaxFF, the structural and the energetic features of LATP were described properly across various compositions – Li occupies more preferentially the interstitial site next to Al than next to Ti. Also, as observed in experimental data, the lattice parameters decrease when Ti is partly substituted by Al because of the smaller size of the Al cation. Using this force field, the diffusion mechanism and the ionic conductivity of Li in LTP and LATP were investigated at T = 300–1100 K. Low ionic conductivity (5.9×10^{-5} S/cm at 300 K) was obtained in LTP as previously reported. In LATP at x=0.2, the ionic conductivity was slightly improved (8.4×10^{-5} S/cm), but it is still below the experimental value, which is on the order of 10^{-4} to 10^{-3} S/cm at x=0.3–0.5. At higher x (higher Al composition), LATP has a configurational diversity due to the Al

substitution and the concomitant insertion of Li. By performing a hybrid MC/MD simulation for LATP at x=0.5, a thermodynamically stable LATP configuration was obtained. The ionic conductivity of this LATP configuration was calculated to be 7.4×10^{-4} S/cm at 300 K, which is one order of magnitude higher than the ionic conductivity for LTP and LATP at x=0.2. This value is in good agreement with our experimental value (2.5×10^{-4} S/cm at 300 K) and the literature values. The composition-dependent ionic conductivity of LATP was successfully demonstrated using the ReaxFF reactive force field, verifying the applicability of the LATP force field for the understanding of Li diffusion and the design of highly Li ion conductive solid electrolytes. Furthermore, our results also demonstrate the feasibility of the MC/MD method in modeling LATP configuration, and provide compelling evidence for the solid solution sensitivity on ionic conductivity.

1. Introduction

In the past few decades, great effort in lithium-ion battery technology has been devoted to enhancing power, capacity and safety.[1] Lithium ion conducting solid electrolytes with various crystalline structures have been investigated extensively as promising alternatives to conventional liquid or polymer electrolytes. The use of inorganic solid electrolytes would greatly improve safety issues associated with flammability of organic liquid electrolytes and lifetime of the battery.[2] In addition, liquid electrolytes allow Li dendrites to grow due to uneven lithium deposition at the anode and can cause internal shorts and several associated safety issues.[3] The suppression of Li dendrite growth not only enhances safety in Li-ion batteries, but may also allow metallic Li to be used as the anode, thereby enhancing energy densities. For these reasons, highly lithium conducting solid electrolytes based on inorganic materials have been intensively investigated.

Both oxide and sulfide-based materials have been considered as solid electrolytes for battery applications. It was reported that the sulfide-based solid electrolytes such as Li_2S-P_2S_5 glass (1.6×10^{-4} S/cm)[4] and $Li_{10}GeP_2S_{12}$ (LGPS) crystal (1.2×10^{-2} S/cm)[5] show high lithium ionic conductivity at room temperature due to the higher ionic radius and higher polarizability of the sulfur ion relative to the oxygen ion. However, LGPS has strong reactivity with air and moisture, forming hazardous H_2S gas when exposed to water. In

addition to the sulfide-solid electrolytes, the oxide-solid electrolytes also exhibit an excellent combination of high conductivity ($\sim 10^{-4}$ S/cm at room temperature), chemical stability against Li metal anodes, and electrochemical stability. For example, garnet-type $Li_7La_3Zr_2O_{12}$ (LLZO)[6, 7] has been attracting attention because of its high conductivity of 3×10^{-4} S/cm and high chemical stability against Li metal. Perovskite-type $Li_{3x}La_{2/3-x}TiO_3$ (LLTO)[8] also exhibits high ionic conductivities at room temperature ($\sim 10^{-3}$ S/cm for x=0.3).

NASICON(Na super ionic conductor)-type materials are known as excellent Li ion conductors, showing high ionic conductivity, low thermal expansion coefficient, low thermal conductivity and low electronic conductivity, and provide great potential as solid electrolytes in all-solid-state lithium batteries.[9, 10] $LiM_2(PO_4)_3$(M=Ti, Zr, Hf, Ge, Sn) systems have been widely studied.[11-15] $LiTi_2(PO_4)_3$ (LTP) is one of the promising solid electrolyte candidates.[10, 16] LTP structure consists of two TiO_6 octahedra linked to three PO_4 tetrahedra. The interstitial channel generated by this TiO_6-PO_4 three-dimensional network provides the conduction path for Li ion transport. Sintered LTP was reported to exhibit relatively poor conductivity of 10^{-6}–10^{-5} S/cm at room temperature, which is not good enough for practical use.[17] However, the ionic conductivity of LTP can be considerably increased when Ti is partly substituted by trivalent metal cations such as Al, Sc, Cr, Fe, Ga, Y and La[16, 18] or when Li concentration increases. The conductivity increases up to 10^{-4}–10^{-3} S/cm for $Li_{1+x}Al_xTi_{2-x}(PO_4)_3$ (LATP) at the most promising compositions, x=0.3-0.5.[16, 19-21] This high ionic conductivity is due to an increasing number of charge carriers as the result of the associated addition of Li to balance the charges and due to the smaller size of the Al cation. The smaller size of Al can result in strong densification of the material, thus making the interstitial void space more appropriate for Li ion diffusion. The ionic conductivity of LATP glass-ceramic obtained from heat-treatment of Li_2O-Al_2O_3-TiO_2-P_2O_5 also exhibits high conductivity of 1.3×10^{-3} S/cm at room temperature.[22] However, the preparation of glass ceramics is complex and the effect of aging on the conductivity is not clearly understood. High conductivity of 2.4×10^{-4} S/cm at room temperature was also reported for $Li_{1.5}Al_{0.5}Ge_{1.5}(PO_4)_3$.[23]

Although remarkable progress has been made over the last few years as described above, optimum solid electrolyte materials have not been identified. Also, because of their complicated crystallographic structures and compositions, the diffusion mechanism of Li

ion has not been elucidated in detail with theory. Thus, tools to perform atomic-scale simulations and examine ionic conductivities are warranted. In the present study, a ReaxFF reactive force field was developed to describe NASICON-type $Li_{1+x}Al_xTi_{2-x}(PO_4)_3$ materials at various aluminum compositions by optimizing the force field parameters against DFT data sets: equations of state of various composite crystal phases and the energy barriers for Li diffusion. To validate the ReaxFF force field and to relate the compositional features of LATP to its ionic conductivities,[20, 24] diffusion constants and ionic conductivities of LTP and LATP at x=0.2 and 0.5 were calculated by performing ReaxFF MD simulations at the temperature range of 300–1100 K. To model LATP at x=0.5, which has a local configurational heterogeneity due to Al and Li distributions, we performed a hybrid MC/MD simulation. The composition-dependent ionic conductivity for LATP is in good agreement with previously reported values. In particular, it was found that the Li ionic conductivity at x=0.5 is greatly enhanced. XRD patterns and ionic conductivity of LATP were compared to experiment and found to be in good agreement. Our simulations allow us to develop a mechanistic description of Li diffusion in LATP.

2. Methodology

2.1 ReaxFF method

ReaxFF has been developed to bridge the gap between quantum mechanical (QM) ab initio and non-reactive empirical force fields.[25] The ReaxFF reactive force field is a bond order dependent force field with instantaneous connectivity for the chemical bonds formed in the atomic local environment. Thus, it is suitable to elucidate not only bond formation and bond-breaking in chemical reactions, but also the reaction process by providing the energetics for various reaction intermediates along a reaction path.[26] The overall system energy is described by physically meaningful many-body empirical potential terms, including bond order-dependent energy terms such as bond, angle and torsion energy which disappear upon bond dissociation, and long range interaction terms such as van der Waals and Coulomb interactions. Since all atom pairs are subject to the long range interactions, a distance-corrected Morse-potential for the van der Waals energy is used to avoid excessively high repulsion at a short distance between atoms sharing a bond. For the

Coulomb interaction, ReaxFF employs the geometry-dependent electronegativity equalization method (EEM) to determine the atomic charges and the electrostatic interactions, and takes into account the shielding between two atoms at a short distance. By using this dynamic charge scheme, ReaxFF can readjust the atomic charges, depending on a local environment generated in ionic or heterogeneous systems. In particular, in multicomponent metal oxides such as LATP, it is important to describe not only various bonding natures such as metallic, covalent and ionic bonds, but also realistic charge dynamics during the reactive events. The classical pairwise potential with a fixed[27] or partially variable charge model (e.g. a shell model)[28-30] has been also widely used for studying Li transport in lithium transition metal oxides at a low computational cost, compared to first-principles density functional theory (DFT) calculations and reactive force fields coupled with the variable charge model, e.g. ReaxFF, the charge-optimized many bond (COMB) potential[31] and a modified embedded atom method (MEAM) with Qeq.[32] However, most previous studies using the classical pairwise potentials have been restricted to a relatively simple chemical structure of specific materials and have not been suitable for covering the wide range of important materials chemistry in lithium battery materials. Since the ReaxFF force field parameters are optimized against typically, a large training data set, the description of the interactions between elements is transferable across phases, reproducing reactive events at the interface between solid, liquid and gas phases. The ReaxFF force field for LATP in the present work was developed to enable simulations involving not only diffusion of Li in a solid crystal phase, but also dynamic behavior of Li in a transient liquid phase (e.g., water) such as dissolution and precipitation of LATP and to understand cold-sintering process,[33-35] which has been very actively employed in the past decades to transform constituent material powders into dense solid materials. All force field parameters describing energy terms are optimized against the QM data and/or experimental values using a single-parameter based parabolic extrapolation method. The details of the ReaxFF force field and its applications are given in our earlier publications.[36-38]

2.2 DFT calculations

For the calculation of Li_xTiO_2 (x=0.25-1.0) crystal phases, the spin-polarized first-principles

DFT calculations were performed using the Vienna ab initio simulation package (VASP)[39] with plane wave basis sets. The DFT calculations use projector augmented wave (PAW)[40] pseudo–potentials and Perdew-Burke-Ernzerhof (PBE)[41] exchange-correlation functional with an energy cutoff of 520 eV. The Brillouin zone is sampled with a 6×8×2 Monkhorst-Pack k-point mesh for monoclinic $Li_{0.25}TiO_2$, a 2×8×6 Monkhorst-Pack[42] k-point mesh for monoclinic $Li_{0.33}TiO_2$, a 4×4×4 Monkhorst-Pack k-point mesh for monoclinic $Li_{0.5}TiO_2$ and a 6×6×4 Monkhorst-Pack k-point mesh for tetragonal $Li_{1.0}TiO_2$. For trigonal $Li_{0.25}TiO_2$ and $Li_{1.0}TiO_2$ crystal phases, a 4×4×2 and a 6×6×4 gamma-centered k-point mesh were used, respectively. Ionic coordinates of all atoms in the crystal phase were allowed to fully relax. To obtain the energy-volume relation, the lattice parameters remained fixed to those of the given lattice parameters in the range from -20 to +30% of the ground state volume while ionic coordinates of atoms were relaxed. Similarly, we calculated the equation of state (EOS) for β-Al_2TiO_5 crystal phase[43] in the volume range of ±20% of the ground state volume using an energy cutoff of 520 eV and a 6×2×2 Monkhorst-Pack k-point mesh for the k-point sampling of Brillouin-zone integrals.

For Li_3PO_4, β- and γ-phases[44] were included in the training set. Ionic relaxation calculations of β- and γ-Li_3PO_4 unit cells were performed, using the ground state bulk lattice parameters taken from literature.[44] Structures were optimized until forces on each atom were less than 0.05 eV/Å. The energy vs. volume data for β-Li_3PO_4 and γ-Li_3PO_4[44] were fitted to a Birch–Murnaghan equation of state, which gave a bulk modulus of 72.45 and 72.02 GPa for β-Li_3PO_4 and γ-Li_3PO_4, respectively. These values are compared well with the reported bulk modulus of 72.2 and 71.9 GPa from Murnaghan equation of state fit.[45] The EOS data sets were generated by compressing and expanding the unit cells within ±15% of the ground state volume and evaluating energy relative to the ground state. The parameters from the Birch–Murnaghan equation of state[46] fit were used to predict the relative energy with respect to the ground state at each volume. The Monkhorst-Pack k-point mesh of 6×6×6 and 6×6×4 were used for β- and γ-Li_3PO_4, respectively, with a plane-wave basis set energy cut-off of 500 eV.

For $AlPO_4$, it has been reported that with increasing pressure, berlinite phase changes to $CrVO_4$, then to a stishovite-type phase and finally to a m-$CaCl_2$.[47-49] In addition, it has been

6

suggested that three more phases (moganite-like, AlVO$_4$, P2$_1$/c) exist between berlinite and CrVO$_4$ phases, based on pressure and temperature.[50] Considering the pressure-temperature range relevant to the current study, the EOS data for the stable berlinite phase, a moganite-like phase and the high pressure CrVO$_4$ phase were included into the training set. The bulk lattice parameters for each phase were taken from the literature.[47, 50] Instead of lattice optimization, the lattice parameters were increased or decreased by the same amount to match the ground state bulk volume reported in literature. Ionic relaxation of these structures was performed. Finally, the parameters[50] of Birch–Murnaghan equation fit were used to calculate the relative energy at different volumes for each phase. The plane-wave basis set energy cut-off was 680 eV and Monkhorst-Pack k-point meshes of 2×2×4, 4×2×6 and 6×4×6 were used for berlinite, moganite-like and CrVO$_4$ phases, respectively.

LTP has a rhombohedral unit cell (space group $R\bar{3}c$) that can be converted into a hexagonal cell. The experimental bulk lattice parameters of the hexagonal unit cell,[51] $a = b =$ 8.5110 Å and c = 20.843 Å, were used as the initial structure with 108 atoms and the ionic coordinates were optimized. To generate the EOS data, the hexagonal unit cell was compressed and expanded within ±15% of the initial volume and ionic relaxation was performed at each volume. The lowest energy structure was found to have bulk lattice parameters $a = b$ = 8.6502 Å and c = 21.1114 Å. The overestimation of the equilibrium volume is a well-known error of the PBE (GGA) functional.[52] The 1.6% overestimation of lattice parameters is within acceptable limit for force field training purposes. The plane-wave basis set energy cut-off for these calculations were 650 eV and a Monkhorst-Pack k-point mesh of 3×3×2 was used.

The valence angle potential energies for Ti-O-Al and Ti-O-P bond angles in gaseous molecular species, i.e., (OH)$_3$Ti-O-Al(OH)$_2$ and (OH)$_3$Ti-O-P(OH) were calculated with Jaguar software package[53] using M06-2X functional with the LACV3P+G** basis set. To obtain the potential energy profile along the valence angle distortion in a molecular fragment, the constrained geometry optimization was applied to Ti-O-Al and Ti-O-P bond angles. The atomic coordinates of all atoms in the system were allowed to fully relax to obtain the optimized structure with fixed valence angle.

2.3 Experimental methods

For comparison of the LATP phase obtained from MC/MD simulations and its ionic conductivity with experiment, LATP films (LIC-GC, LATP/SiO$_2$, 19 mm diameter × 160 μm thickness) supplied from Ohara Inc. were used. X-ray diffraction patterns of LATP were collected using a PANalytical Empyrean XRD with Cu-Ka radiation (λ = 1.54059 Å) in the 2θ range from 10 to 70° in steps of 0.026°. To obtain the ionic conductivity of LATP, we measured impedance spectra in the temperature range of 273 – 373 K, using a Solatron Ametek Modulab with an AC amplitude of 10 mV in the range of 10^{-1}–10^6 Hz after sputtering 100 nm Au electrodes on both sides of the sample.

3. Results and discussion

3.1 ReaxFF force field development

Based on our earlier developed metal oxide force fields for Al/O,[54] Ti/O,[55] Li/O[56], Al/O/Li[57] and phosphate,[58] in the present work we merged and expanded these force fields into one large comprehensive force field to describe various combinations of ternary metal oxides and metal phosphates, e.g., Al/O/Li, Ti/O/Li, Al/O/Ti, Li/O/P, Al/O/P and Ti/O/P in LATP materials. The extension of the oxide force fields to one complex ternary metal oxide force field is relatively straightforward, requiring only a few parameters to be optimized with an explicit training data set – the van der Waals long range interactions for Ti-Li, Al-Li, Ti-Al, Al-P, Li-P and Ti-P and the valence angle parameters for Ti-O-Li, Al-O-Li, Ti-O-Al, Al-O-P, Li-O-P and Ti-O-P valence angles were parameterized using DFT data sets, including equations of state and heats of formation for the oxides and phosphate crystal phases, hydrolysis reactions of molecular fragments of (OH)$_3$Ti-O-P(OH)$_3$ and (OH)$_3$Ti-O-Al(OH)$_2$, and Li diffusion pathways in rutile-TiO$_2$ and LTP via interstitial and vacancy sites. Since the Li/O force field has been recently improved by adding the solvation in liquid phase to the training data set,[56] in this work, we also re-optimized the van der Waals long range interaction terms for Al/Li and Al-O-Li valence angle parameters to reproduce equations of state for LiAlO$_2$ alloy oxide phases of reference [57].

Equations of state – the energy-volume relationship – for ternary oxide crystals such as Li$_x$TiO$_2$ (x=0.25-1.0), α-, β-, γ-LiAlO$_2$ and β-Al$_2$TiO$_5$ are plotted in Fig. 1. The volume of the crystal phase was expanded and compressed in the range from -30% up to +40% of the

ground state volume. As shown in Fig. 1, Li_xTiO_2 phases are placed close to each other with formation energies of -7.8 to -3.1 kcal/mol in ReaxFF and -8.0 to -0.99 kcal/mol in DFT when rutile-TiO_2 and bcc Li are used as references. ReaxFF slightly overestimates the heat of formation of $Li_{0.5}TiO_2$ (monoclinic) and $Li_{0.25}TiO_2$ (trigonal) by about 2 kcal/mol, however the relative stability between the crystal phases is well reproduced.

β-Al_2TiO_5, which is a composite of α-Al_2O_3 and rutile-TiO_2 is known to be unstable and decompose into α-Al_2O_3 and rutile-TiO_2 under T = 1553 K.[43] The density of this ternary oxide is 3.61 g/cm^3 in both ReaxFF and DFT, which is lower than α-Al_2O_3 (3.87 g/cm^3) and rutile-TiO_2 (4.19 g/cm^3), thus the formation of this phase is accompanied by an increase of molar volume. The heat of formation of β-Al_2TiO_5 is -0.02 kcal/mol in ReaxFF, which indicates that there is negligible energy to gain by the formation of Al_2TiO_5 phase. This is in excellent agreement with the DFT value (-0.01 kcal/mol) and the observation in the earlier work.[43] Valence angle parameters for Ti-O-Al bond angle were fitted against the potential energy profile for a broad range of Ti-O-Al valence angle distortion in $(OH)_3Ti$-O-$Al(OH)_2$ fragment. As shown in Fig. 2(a), the potential energy change responding to the valence angle change is well reproduced in ReaxFF.

$LiAlO_2$ oxide, in particular γ-$LiAlO_2$ has been implemented in many battery applications such as coating for lithium-conducting electrodes or an additive in composite electrolytes.[59, 60] The mechanical responses of $LiAlO_2$ under compression and expansion in different orientations were included for the optimization of Al/O/Li force field parameters. The formation energies for α-$LiAlO_2$, β-$LiAlO_2$ and γ-$LiAlO_2$ phases in DFT are -72.5, -73.0 and -73.1 kcal/mol, respectively, when fcc Al, bcc Li and molecular oxygen are used as references. The corresponding ReaxFF values are -76.7, -78.8 and -79.2 kcal/mol, respectively. For comparison of the thermodynamic stability with Li_xTiO_2 and Al_2TiO_5, formation energies can be also calculated using α-Al_2O_3 and Li_2O oxides as references – the formation energies with these references are -8.8, -11.0 and -11.3 kcal/mol in ReaxFF and -10.2, -10.7 and -10.8 kcal/mol in DFT, which indicates that $LiAlO_2$ oxides are thermodynamically more stable than Li_xTiO_2 and Al_2TiO_5 oxides. As shown in Fig. 1, the energy–volume relationship and the relative stability of the oxide crystal phases are well reproduced in ReaxFF.
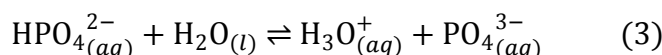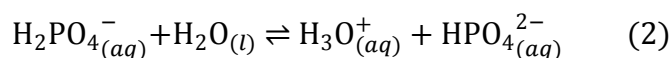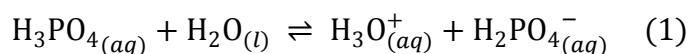
Metal phosphates are also important for describing LATP materials since LATP

structure is a three-dimensional network built of Ti(or Al)O_6 octahedra linked to PO_4 tetrahedra. In Fig. 1, it is shown that equations of state for berlinite, moganite-like and $CrVO_4$–$AlPO_4$ phases and β, γ–Li_3PO_4 phases are well reproduced in ReaxFF. The formation energy of $AlPO_4$ with references of α-Al_2O_3 and P_2O_5 is calculated to be -5.3 for berlinite phase, -5.5 for moganite-like phase and -3.3 kcal/mol for less stable $CrVO_4$ phase, which is well comparable with the DFT values, -6.2 kcal/mol for both berlinite and moganite-like phases and -3.9 kcal/mol for $CrVO_4$ phase. We note that the formation energy for Li_3PO_4 is overestimated in ReaxFF (-22.9 kcal/mol in ReaxFF and -12.1 kcal/mol in DFT), probably affecting the thermodynamic stability of LATP as well. However, since Li is placed at the interstitial site of the three dimensional network in LATP, the lithium phosphate may not be the structure directly observed in LATP. Also because the research focus in the recent work is Li diffusion behavior such as the energy barriers along the diffusion pathways in LATP, the overestimation of Li_3PO_4 crystal phase would be less concerned. Lastly, titanium (IV) phosphate is of interest for their chemical and physical properties as ionic conductors or catalysts. Since to the author's knowledge, the crystal phase and structure of titanium phosphate are not well known, as shown in Fig. 2(b), the potential energy profile along the Ti-O-P valence angle distortion in a molecular fragment of $(OH)_3Ti$-O-$P(OH)_3$ was used to optimize Ti-P van der Waals interaction terms and Ti-O-P valence angle parameters. Overall the thermodynamic stability of oxides and phosphates describing LATP is in good agreement with DFT.

Recently, it has been shown that LAGP could be sintered into solid monolithic materials and also with polymer-composites through cold sintering.[33, 61] Here a dense material can be obtained through the use of a transient liquid phase that enables dissolution and precipitation to enhance the densification process. To address the potential application of the LATP force field to cold-sintering process, we here also consider the hydrolysis reactivity between water and LATP. Hydrolysis of oxide and phosphate at the interface between LATP and water can play a major role in determining the morphology and chemical and physical properties of the interface or the grain boundary at the contact with water. To describe such reaction correctly, it is essential to obtain a quantitative description of the corresponding reaction. The gas phase hydrolysis reaction of $(OH)_3Ti$-O-$P(OH)_3$ and

$(OH)_3Ti-O-Al(OH)_2$ molecular fragments produces $Ti(OH)_4$, H_3PO_4 and $Al(OH)_3$, respectively. In ReaxFF, the reaction energy is -14.3 kcal/mol for $(OH)_3Ti-O-P(OH)_3$ and -10.3 kcal/mol for $(OH)_3Ti-O-Al(OH)_2$, which is in good agreement with the DFT values, -13.0 kcal/mol and -12.1 kcal/mol, respectively.

Furthermore, in order to describe the reactions involving phosphoric acid and hydrogen phosphate derivatives in water, we included dissociation energies of phosphoric acid into the training set. Phosphoric acid is a weak acid with the chemical formula H_3PO_4, which dissociates in the following manner:

$$H_3PO_{4(aq)} + H_2O_{(l)} \rightleftharpoons H_3O^+_{(aq)} + H_2PO^-_{4(aq)} \quad (1)$$

$$H_2PO^-_{4(aq)} + H_2O_{(l)} \rightleftharpoons H_3O^+_{(aq)} + HPO^{2-}_{4(aq)} \quad (2)$$

$$HPO^{2-}_{4(aq)} + H_2O_{(l)} \rightleftharpoons H_3O^+_{(aq)} + PO^{3-}_{4(aq)} \quad (3)$$

The dissociations of phosphoric acid require extremely long simulation times which are not reachable by normal molecular dynamics simulations. Therefore, sampling methods are employed to investigate the dissociation at atomistic level. Metadynamics is a commonly used sampling method to accelerate rare events (e.g. dissociation of acids) by preventing the system to visit previously sampled configurations.[62] The metadynamics has been used to calculate the dissociation constants of acids by several researchers.[63-65] In this work, we used ReaxFF-based metadynamics simulations to calculate the three dissociation reactions of phosphoric acid. The initial configuration of the system was generated by solvating one phosphoric acid molecule in 60 water molecules in a cubic box with a periodic boundary condition. The side length of the box (12.39 Å) was determined by keeping the water density in the system at 1 g/cm³. The initial system was equilibrated in the isobaric-isothermal (NPT) ensemble for 1 ns before metadynamics was applied. The temperature and pressure were controlled by the Berendsen thermostat and barostat, and kept constant, respectively, at 300K and at 0.1 MPa.[66] We used a 0.25 fs time step to integrate Newton's equation of motion using Velocity-Verlet algorithm. Starting configuration for metadynamics simulations was taken from the last step of the equilibration simulation.

We defined four separate collective variables (CVs) for each of the oxygens in phosphoric acid, namely, CV1, CV2 and CV3 for hydroxyl oxygens, and CV4 for double

11

bonded oxygen. The CVs were defined as the coordination of phosphoric acid oxygens by hydrogen atoms in the system (eq. 4).

$$S_{OH} = \sum_{j=1,...,N_H} \frac{1 - \left(\dfrac{R_{OH_j} - d_0}{R_0}\right)^6}{1 - \left(\dfrac{R_{OH_j} - d_0}{R_0}\right)^{12}} \qquad (4)$$

where N_H is the number of hydrogen atoms and R_{OH_j} is the distance between oxygen and j^{th} hydrogen atoms. We set the parameters $R_0 = 0.3$ Å and $d_0 = 1.0$ Å.

The sampling was performed in three stages. During the sampling, the Gaussian parameters for height and width were chosen as 0.3 kcal/mol and 0.01 Å, respectively. The Gaussian potential was deposited with a time step of 50 fs to the selected CV depending on the sampling stage. An upper wall was applied to the selected CVs depending on the stage to prevent them being protonated by applying a restraining potential in the form shown in eq. 5.

$$V_{wall}(S_{OH}) = \kappa\left(S_{OH} - S_{OH_{limit}}\right)^4 \qquad (5)$$

where S_{OH} is the value of the selected CV and $S_{OH_{limit}}$ is the maximum allowed value of the selected CV. The parameters are set as $S_{OH_{limit}} = 0.01$ and $\kappa = 100$. In the first stage, the upper wall was applied to CV4 to prevent protonation and the Gaussians were deposited to CV1 to trigger the dissociation. Since the purpose was to estimate the energy barriers of dissociations, each stage ended after hydrogen atom detached from the oxygen atom and formed a hydronium ion, and the hydronium ion has no interaction with residual conjugate base ion. In the second stage, another upper wall was activated for CV1 and the Gaussians were deposited to CV2. In the last stage, another upper wall was applied to CV2 and the Gaussians were added to CV3. At the end of each stage, we checked if the entire free energy surface was explored in CV space.

The corresponding free-energy profile in Fig. 3 shows well-defined energy barriers for each dissociation reaction in eqs. (1) – (3). The pK_a value for each of the dissociations was estimated using the free-energy and the formula, $pK_a = \Delta G/2.303RT$.[63, 65] The pK_a values for phosphoric acid dissociation reactions were calculated as $pK_{a_1} \approx 1.1$, $pK_{a_2} \approx 6.3$ and

12

$pK_{a_3} \approx 11.4$. The experimental values of dissociation constants are 2.1, 7.2 and 12.6 at 298.15 K, respectively.[67] The difference between computed and experimental pK_a values corresponds to an energy difference approximately as small as 1.36 kcal/mol. This energy difference is reasonable, compared to the errors in other models,[68] therefore, it is safe to mention that the dissociation trend is in agreement with experiment.

To validate the ReaxFF force field for LATP, we studied the structural and the energetic characteristics of bulk LATP. The unit cell of LTP ($a = b = 8.647$ Å, $c = 21.103$ Å, as shown in Fig. 4a) adopts the well-known NASICON type structure which consists of a three-dimensional network built of TiO_6 octahedra and PO_4 tetrahedra and six Li ions at M_1 site. The 108-atom unit cell contains six formula units. For LATP at x=0.2, one Ti in the unit cell is substituted by Al and one Li is added to the $M_{1/2}$ interstitial site for charge compensation as shown in Fig. 4(b). There are six equivalent $M_{1/2}$ sites per one M_1 site. By adding additional Li to one of the $M_{1/2}$ interstitial sites, Li atom that was initially on M_1 site also shifts to the facing $M_{1/2}$ interstitial site, generating two interstitial Li atoms – Li(4) and Li(7) in Fig. 4(b). Unlike LTP, there are two distinguishable $M_{1/2}$ sites available for Li in LATP – one is the site next to Al and the other is the site next to Ti. It has been reported that the site next to Al is thermodynamically more stable than the site next to Ti by 4.6 kcal/mol.[69] In ReaxFF, Li is also preferentially located next to Al with the energy difference of 6.3 kcal/mol from $M_{1/2}$ site next to Ti. Since the interstitial Li next to Al is energetically more favorable, it is expected that Li stays longer near Al than Ti.

Fig. 5 shows equations of state for LTP and LATP (x=0.2). The ReaxFF potential energies at different densities of LTP are well compared to the DFT data. In LATP at x=0.2 ($a = b = 8.639$ Å, $c = 21.084$ Å), the equation of state shifts slightly toward lower densities (99.65% of LTP) and is less sensitive to large volume changes. When Ti is substituted by Al in LTP, the system lattice parameters assuredly decrease due to the smaller size of the Al cation, probably making the interstitial channel more appropriate for Li diffusion. However, because Al is lighter than Ti, the density becomes slightly lower than that of LTP as observed in experiment (99.76% of LTP).[19] The composition-dependent lattice parameters are well reproduced in ReaxFF.

Understanding the diffusion behavior of Li in LATP would help understanding the

composition-dependent ionic conductivity of LATP and modeling highly Li ion conductive LATP materials at x=0.3–0.5. As a first step, we discuss Li diffusion in rutile-TiO$_2$. Rutile-TiO$_2$ structure consists of TiO$_6$ octahedra linked via oxygen, generating one dimensional void channel in the *c*-direction. The thermodynamically preferred site for Li insertion has been known to be the octahedral site surrounded by six oxygen atoms. Energetically efficient Li diffusion in rutile-TiO$_2$ can take place along the path connecting these two octahedral sites, which is the channel parallel to the *c*-axis. In order to investigate the diffusion of Li in TiO$_2$, an isolated Li atom was inserted into the octahedral interstitial site of a (2 × 2 × 2) supercell and the potential energy profile for Li migration was obtained along this diffusion pathway. As shown in Fig. 6, the energy barrier is very low, 0.8 kcal/mol in ReaxFF, which is in excellent agreement with the DFT value (1.1 kcal/mol).[70] Low energy barrier for Li diffusion indicates that Li in rutile-TiO$_2$ can diffuse fast even at low temperature.

LTP and LATP structure consists of a TiO$_6$–PO$_4$ three-dimensional diffusion network, providing a potentially efficient ionic conductivity channel. Li transport can take place through this channel by a series of Li migration via interstitial or vacancy sites. For example, in LTP rhombohedral structure, all Li atoms are placed at M$_1$ sites surrounded by six oxygen atoms. In the presence of vacancy, a three-dimensional network linking one M$_1$ site to another M$_1$ site throughout the LTP crystal provides a Li diffusion channel. Due to the complexity of the structure, the diffusion of Li in LTP has been studied by a few computational methods – from MM and MD simulations,[71] the activation energy for Li diffusion via vacancy was estimated to be 6.9 kcal/mol. In DFT,[69] the activation energies for Li diffusion via vacancy and interstitial sites in LTP were reported to be 9.4 kcal/mol and 4.4 kcal/mol, respectively.

For comparison with published work, we modeled a LTP system of a 108-atom unit cell and created one vacancy at M$_1$ site as shown in Fig. 7. The energy barrier for the vacancy diffusion is 8.3 kcal/mol in ReaxFF, which is in good agreement with the DFT value (9.4 kcal/mol). While Li diffusion via vacancy can take place by a simple mechanism of hopping from one M$_1$ site to the neighboring M$_1$ site, the diffusion pathway through interstitial sites can be more complex because three Li atoms at M$_{1/2}$ sites are involved in the diffusion process, performing concurrent migrations. For example, the insertion of Li into M$_{1/2}$ site

induces migration of the neighboring Li at M_1 site to another $M_{1/2}$ site, consequently generating two Li atoms at $M_{1/2}$ site, which is similar to Li(4) and Li(7) in Fig. 4(b). When Li(7) at $M_{1/2}$ site diffuses toward Li(3) at M_1 site through the three-dimensional diffusion channel, Li(4) at $M_{1/2}$ site diffuses concurrently back to M_1 site. As Li(7) approaches the interstitial site next to Li(3), Li(3) also starts migration to the facing $M_{1/2}$ site, finally generating two $M_{1/2}$ Li atoms (Li(3) and Li(7)). The diffusion process through interstitial sites can be more important in LATP because additional Li atoms have to exist for charge balance. In DFT work,[69] the activation energy for the interstitial diffusion in LTP was reported to be 4.4 kcal/mol, which is only a half of the activation energy for the vacancy diffusion. Since the interstitial diffusion is kinetically more efficient than the vacancy diffusion, it is expected that the interstitial Li diffusion would be more dominant, in particular at low temperature. In ReaxFF, the energy barrier is 6.0 kcal/mol, which is slightly higher than the DFT value but lower than the energy barrier for the vacancy diffusion, making the interstitial diffusion to be dominant as is expected in DFT.

In the current ReaxFF force field, the energetic and the structural features of LTP and LATP are reproduced properly, agreeing well with the DFT data. In addition, Li diffusion through interstitial and vacancy sites, which is essential to study the ionic conductivity of LATP, is also in good agreement with the earlier works.

3.2 MD simulation for Li diffusion in bulk LATP (x=0-0.5)

According to earlier experimental works,[16, 19, 72, 73] the substitution of Ti by Al in LTP enhances significantly the Li ionic conductivity. Depending on the synthesis and sintering conditions, the total ionic conductivity of LATP was reported to vary between 10^{-4} and 10^{-3} S/cm.[19, 22, 74-78] In particular, it was reported that significantly high Li ion diffusivity can be achieved in LATP at x=0.3-0.5.[16, 19-21, 73, 79] This may indicate that the diffusion behavior of Li is affected by the composition. Thus, understanding of the diffusion process in LATP at different compositions is essential for understanding its high ionic conductivity. The diffusion mechanism of Li in LTP and LATP has not been well elucidated in detail in theory due to its complicated structure and composition. Atomistic scale MD simulation can be an essential tool to study the Li diffusion mechanism and find the relation between LATP composition and Li diffusion. Using the ReaxFF force field developed in the present work,

we investigated the Li diffusion in LTP and LATP at x=0.2 and 0.5.

First, we performed MD simulations for Li diffusion in LTP without defect – all six Li atoms in a 108-atom unit cell are placed at M_1 site and there is no Li atom at $M_{1/2}$ site. A (4 × 4 × 2) supercell was generated using this unit cell to perform MD simulations at T = 300–1100 K. The system was equilibrated at 300 K, 400 K, 500 K, 700 K, 900 K and 1100 K for 100 ps under NVT ensemble using Berendsen thermostat with a relaxation constant of 100 fs. To collect diffusion trajectories for analysis, NVT MD simulations were performed for 400 ps, using Berendsen thermostat with a weak thermostat coupling of a relaxation constant of 1000 fs. For parallel ReaxFF MD simulations, we used the ADF/ReaxFF implementation.[80]

Li diffusion constant at each temperature is obtained from the slope of the averaged mean square displacement (MSD) using Einstein's relation.

$$MSD(t) = \frac{1}{n}\sum_{i}^{n}\langle[r_i(t) - r_i(0)]^2\rangle \qquad (6)$$

$$MSD(t) = 6Dt \qquad (7)$$

where D is the diffusion constant of Li at a given temperature (T), n is the number of Li in the system and $r_i(t)$ is the position of Li at time t. The MSD of each Li atom is calculated using its position as a function of time. The MSDs of all Li atoms are summed and averaged to extract the diffusion coefficient. For LTP, the diffusion constant is very low, 2.1×10^{-9} cm^2/s at 300 K. From the diffusion constants calculated from MSDs at different temperatures, the plot of ln D vs. 1/T is shown in Fig. 8. Since diffusion in the given temperature range exhibits Arrhenian behavior, a fit to $D = D_0\exp(-E_a/RT)$ can give an activation energy. From the slope of the fit, the activation energy for Li diffusion in defect-free LTP is estimated to be 3.8 kcal/mol, which is close to the DFT value (4.4 kcal/mol) for the diffusion via interstitial sites in LTP. However, since there is no interstitial Li at $M_{1/2}$ site at the initial configuration, diffusion via interstitial sites cannot explain the diffusion in defect-free LTP. To understand the diffusion process in LTP, the decomposed MSD was analyzed. The decomposition of the MSD in Fig. 9 shows that the dominant diffusion occurs along the *ab*-plane rather than the *c*-axis at 300–900 K, e.g., at 300 K, D = 2.1×10^{-9} cm^2/s,

D_{ab} = 3.1 × 10⁻⁹ cm²/s and D_c = 2.7 × 10⁻¹⁰ cm²/s and at 900 K, D = 9.4 × 10⁻⁸ cm²/s, D_{ab} = 1.2 × 10⁻⁷ cm²/s and D_c = 3.9 × 10⁻⁸ cm²/s. This indicates that Li does not migrate toward another M_1 site and/or $M_{1/2}$ site along the c-axis but diffuses relatively easily on ab-plane – the migration within six $M_{1/2}$ sites surrounding one M_1 site or the migration from $M_{1/2}$ site to the neighboring M_1 site. The diffusion pathway of Li is visualized in Fig. 10(a) by tracking the trajectories of several Li atoms over time at 900 K. It is observed that the diffusion of Li takes place within $M_{1/2}$ sites on ab-plane. Due to the low diffusion constants, its motion is still limited to around its initial position. However, at high temperature, it is possible that LTP has the local lattice distortion caused by temperature. Temperature induced defect structure may allow Li to diffuse along the locally generated energy barriers in the c-direction. At 1100 K, diffusion constants in all three directions are obtained within the same order of magnitude (D_{ab} = 3.1 × 10⁻⁷ cm²/s and D_c = 2.7 × 10⁻⁷ cm²/s).

Based on the Nernst-Einstein equation, the Li ionic conductivity (σ) can be calculated from the Li diffusion constant, the system temperature and the concentration of Li.

$$\sigma = \frac{F^2 n_0 q^2}{RT} D \qquad (8)$$

where F is the Faraday constant, n_0 is the number of Li per volume of the system, q is the ion charge, R is the gas constant and D is the diffusion constant of Li at a given temperature (T). The ionic conductivity of LTP from this equation is estimated to be 5.9 × 10⁻⁵ S/cm at 300 K, which is within the same order of magnitude of the experimental value (7.2 × 10⁻⁵ S/cm at 300 K).[17]

For the system of LTP that includes point vacancies, two out of six Li atoms at M_1 site were randomly chosen to be removed from a 108-atom unit cell as shown in Fig. 11. MD simulations were carried out in a (4 × 4 × 2) supercell and the diffusion constants were calculated at T = 500–1300 K. Unlike LTP without vacancy, it was observed from the ln D vs. 1/T plot that two types of diffusion take place at low and high temperature. At low temperature below 700 K, the diffusion constants appear to lie very close to the linear fit of the defect-free LTP. This may indicate that the vacancy defect which has a high energy barrier for diffusion does not affect much the low-temperature diffusion. The diffusion constants are placed within the same order of magnitude of those in defect-free LTP. From

the decomposition of the MSD, it was observed that at T ≤ 700 K, Li diffusion occurs dominantly on *ab*-plane with a slightly higher diffusion constant– at 500 K, D_{ab} = 2.8 × 10^{-8} cm^2/s and D_c = 1.9 × 10^{-8} cm^2/s. Due to the distortion around the vacancy defect, slow diffusion along the *c*-axis that was observed in the low temperature diffusion of the defect-free LTP is less significant. On the other hand, at high temperature range (> 700 K), Li can overcome the energetic cost for the vacancy diffusion from one M_1 to another M_1 along the *c*-axis. The slope of the ln D vs. 1/T plot is steeper than that of the low temperature region as shown in Fig. 8. The energy barrier for Li diffusion is 10.8 kcal/mol, which is comparable to the DFT value (9.4 kcal/mol) for the vacancy diffusion in LTP with a single vacancy. At the temperature above 900 K, the diffusion constants are two to three times higher than those of the defect-free LTP because of the activated three-dimensional diffusion – at 900 K, D = 3.0 × 10^{-7} cm^2/s with vacancy and 0.94 × 10^{-7} cm^2/s without vacancy, and at 1100 K, D = 5.5 × 10^{-7} cm^2/s with vacancy and 2.9 × 10^{-7} cm^2/s without vacancy.

Ionic conductivity can be enhanced by increasing the concentration of Li (the higher number of charge carriers) and by providing more efficient diffusion pathway. To understand the composition-dependent ionic conductivity of LATP, we investigated the diffusion behavior of Li in LATP at x=0.2 and x=0.5. For the system of LATP at x=0.2, one out of 12 Ti atoms in a 108-atom LTP unit cell was replaced by Al. For charge balance, one additional Li atom was added to the $M_{1/2}$ site next to Al, which is known to be more stable than that next to Ti. We note that an extra Li atom can generate two interstitial Li atoms. In LATP at x=0.2, about 29% Li atoms are positioned at $M_{1/2}$ interstitial site. The 109-atom unit cell of LATP was expanded to generate a (4 × 4 × 2) supercell for the MD simulation. While the configuration of LATP at x=0.2 has been already well determined by DFT studies, the configuration of LATP at higher Al composition has not been known yet. The three-dimensional distribution of Al and interstitial Li atoms can play a key role in generating locally heterogeneous various LATP materials. Thus, it is critical to predict and model an appropriate configuration of LATP for studying the diffusion behavior. Since there are a number of possible configurations for LATP, depending on Al and Li atomic distributions, it is inherently challenging to fully characterize both Al and Li configurations. Although it is also of great interest to study the Li configuration, sampling a number of possible Li interstitial sites is computationally very expensive. Thereby, we only searched the

thermodynamically stable Al configuration in the given Li distribution at a reduced computational cost. To predict the thermodynamic stability of various Al atomic configurations in LATP at x=0.5, we performed a hybrid MC/MD simulation. The initial configuration was constructed by replacing randomly chosen three Ti atoms by Al atoms in a 108-atom LTP unit cell and adding three additional Li atoms to $M_{1/2}$ interstitial sites next to Al site. In this system, more Li atoms (about 67% Li at $M_{1/2}$ interstitial site) are available for diffusion via interstitial sites. This 111-atom unit cell was expanded to generate a (4 × 4 × 2) supercell. Using this initial configuration, we performed a MC/MD simulation to determine the Al configuration. In the MC/MD simulation, two metal atoms (Ti and Al) are allowed to exchange the position with an identity swap move. All accepted configurations were stored during the simulation and the last configuration was taken to give a good representation of the Al configuration paired with the given Li configuration. Fig. 12 shows the potential energy data points of the configurations generated during the swap trials and the snapshot of the final LATP configuration determined by the MC/MD simulation. From the final configuration of LATP, it was observed that Al atoms prefer to be clustered on *ab*-plane and not to be isolated by neighboring Ti atoms. For comparison of the LATP crystal structure from the MC/MD simulation with LATP materials in experiment, we calculated X-ray diffraction patterns (XRD) of LTP and LATP at x=0.5 using X-ray and electron scattering factors fitted to the analytic function and the coefficients for the fit.[81, 82] In Fig. 13(a, b), in comparison with LTP, the peaks in LATP shift slightly toward the higher theta angles because the lattice parameters decrease due to the smaller size of the Al cation. Since the lattice parameters in ReaxFF are slightly larger than those reported in experiments, it is supposed that overall the peaks of patterns in ReaxFF shift slightly toward lower theta angles than the peaks measured by experiment as shown in Fig. 13(c). Except for the shift originated from the lattice parameter difference, the intense peaks of patterns for LATP from the MC/MD simulation agree well with those in our experiment and earlier work.[19, 83] This LATP configuration was taken for the study of Li diffusion at T = 300–1100 K.

From the analysis of the MD simulation data, the diffusion constant of LATP at x=0.2 was calculated to be 2.6 × 10^{-9} cm^2/s at 300 K, which is slightly higher than that of LTP. The estimated activation energy from the ln D vs. 1/T plot (Fig. 14) is 3.9 kcal/mol. This value is very close to the activation energy for either the interstitial diffusion in LTP (4.4 kcal/mol in

DFT) or the diffusion in defect-free LTP (3.8 kcal/mol). We note that the energy barrier of 4.4 kcal/mol was calculated in LTP with interstitial Li atoms at $M_{1/2}$ site next to Ti. In LATP, interstitial Li atoms are initially positioned at more stable $M_{1/2}$ site next to Al (by 6.3 kcal/mol). This may indicate that the energy barrier for the interstitial diffusion can be higher than 4.4 kcal/mol. In addition, at x=0.2, only 29% of the total Li in the system are available for the interstitial diffusion and 71% Li may behave similar to Li in defect-free LTP. It was found that at low temperature, the diffusion constant along the *c*-axis is lower than that along the *ab*-plane ($D_{ab} = 3.4 \times 10^{-9}$ S/cm and $D_c = 1.2 \times 10^{-9}$ S/cm at 300 K), which is similar to the observation in defect-free LTP. Since the diffusion constants are within the same order of magnitude, this may imply that the three-dimensional diffusion via interstitial sites partly contributes to overall Li diffusion as well. The ionic conductivity, 8.4 $\times 10^{-5}$ S/cm at 300 K is only slightly higher than that of LTP and lower than the reported ionic conductivity (10^{-4} to 10^{-3} S/cm) at x=0.3-0.5.

A drastic change in Li diffusion and ionic conductivity was observed at the composition of x=0.5. The diffusion constant was calculated to be 1.7×10^{-8} cm^2/s at 300 K with the corresponding ionic conductivity of 7.4×10^{-4} S/cm, which is one order of magnitude higher than that of LATP at x=0.2. This value is close to the experimentally reported ionic conductivities at 300 K – 7×10^{-4} S/cm in $Li_{1.3}Al_{0.3}Ti_{1.7}(PO_4)_3$[16] and 2.5×10^{-4} S/cm from our measurement by impedance spectroscopy. It is shown from Fig. 14 that the Li diffusion is significantly enhanced at low temperature. As the number of Li at $M_{1/2}$ site increases (67%), the contribution of the three-dimensional interstitial diffusion to overall diffusion can also increase. The diffusion constant along the *c*-axis is comparable to that along the *ab*-plane over the temperature range of 300 K to 1100 K – $D_{ab} = 1.8 \times 10^{-8}$ cm^2/s and $D_c = 1.5 \times 10^{-8}$ cm^2/s at 300 K and $D_{ab} = 1.8 \times 10^{-7}$ cm^2/s and $D_c = 1.9 \times 10^{-7}$ cm^2/s at 1100 K. The three-dimensional diffusion pathway of Li at 1100 K is shown in Fig. 10(b). In comparison with the diffusion behavior of Li in LTP, interstitial Li atoms migrate from one $M_{1/2}$ to the other $M_{1/2}$ along the *c*-axis as indicated by the decomposed diffusion constants. This may suggest that the three-dimensional diffusion of interstitial Li atoms improves the diffusion constant and the ionic conductivity. The energy barrier for Li diffusion at x=0.5 (1.9 kcal/mol) is lower than that at x=0.2 and experimental values (5.5 kcal/mol from our measurement at 273–373 K in Fig. 15, 3.7–3.9 kcal/mol from NMR at low temperature range[21] and 6.0

Physical Chemistry Chemical Physics

kcal/mol from impedance spectroscopy[21]). Due to the heterogeneity induced by the Al distribution, LATP with higher Al composition can have more diverse local configurations and may have the various local minima with low energy barriers, resulting in the low energy barrier for the overall diffusion. We note that at high temperature, the diffusion constants for LATP are placed within the same order of magnitude of those in LATP (x=0.2). When long-range diffusion takes place through interstitial sites, interstitial Li has a higher chance to find and stay longer at thermodynamically more stable sites near Al. This may retard the diffusion, resulting in low diffusion constant.

In summary, the diffusion constant, the activation energy and the ionic conductivity in LTP and LATP at x=0.2, 0.5 are calculated in good agreement with the values reported in experiment and theory. These results demonstrate the composition-dependent ionic conductivity of LATP – from 5.9×10^{-5} S/cm in LTP (x=0) to 7.4×10^{-4} S/cm in LATP (x=0.5).

4. Conclusions

In the present work, we developed a ReaxFF force field for the study of NASICON-type $Li_{1+x}Al_xTi_{2-x}(PO_4)_3$ (LATP) solid electrolyte materials. Using ReaxFF, the structural and the energetic features of LATP were reproduced properly – Li occupies more favorably the interstitial site next to Al than next to Ti. In addition, it was found that the lattice parameters decrease when Ti is partly substituted by Al in LATP, due to the smaller size of the trivalent Al cation. This is in good agreement with the observation in experiment.

To validate the ReaxFF force field for LATP, we studied Li diffusion in LTP and LATP at x=0.2 and 0.5. The ionic conductivity of LTP is 5.9×10^{-5} S/cm at 300 K, which is within the same order of magnitude of the experimental value (7.2×10^{-5} S/cm). In LATP at x=0.2, the interstitial diffusion (29% Li) contributes only partially to the overall diffusion and the activation energy (3.9 kcal/mol) is close to the activation energy in defect-free LTP (3.8 kcal/mol). The corresponding ionic conductivity is 8.4×10^{-5} S/cm at 300 K, which is slightly higher than that of LTP, but lower than the experimentally reported optimum ionic conductivity for LATP at x=0.3-0.5 ($10^{-4} \sim 10^{-3}$ S/cm).

Higher Al composition of LATP induces a configurational diversity, due to a number of possible Al and Li distributions. Since locally heterogeneous LATP materials by the Li

and/or Al configurations can affect Li diffusion, it is critical to model an appropriate LATP configuration. Due to the computational cost, we searched only the most stable Al distribution at the given Li distribution by performing a hybrid MC/MD simulation. The ionic conductivity for the LATP configuration determined from the MC/MD simulation was estimated to be 7.4×10^{-4} S/cm at 300 K, which is one order of magnitude higher than those in LTP and LATP (x=0.2) and in the same range of experimental values (10^{-4} to 10^{-3} S/cm). Due to the heterogeneity induced by the Al distribution, LATP can have more diverse local structures with the various local minima. This can result in the low energy barrier for the overall diffusion (1.9 kcal/mol).

In summary, the composition-dependent ionic conductivity of LATP was demonstrated using the ReaxFF reactive force field in good agreement with the earlier works. These results can provide important insights for the understanding of Li diffusion mechanism and verify the applicability of the LATP force field for designing of highly Li ion conductive LATP materials.

Supporting Information

ReaxFF reactive force field parameters for the solid electrolyte LATP materials.

Conflicts of Interest

The authors declare no competing financial interest.

Acknowledgements

Notes and references

1.   J. M. Tarascon and M. Armand, *Nature*, 2001, 414, 359-367.
2.   W. Li, J. R. Dahn and D. S. Wainwright, *Science*, 1994, 264, 1115-1118.

3.   S. Chandrashekar, N. M. Trease, H. J. Chang, L. S. Du, C. P. Grey and A. Jerschow, *Nat Mater*, 2012, 11, 311-315.

4.   K. Minami, F. Mizuno, A. Hayashi and M. Tatsumisago, *Solid State Ionics*, 2007, 178, 837-841.

5.   N. Kamaya, K. Homma, Y. Yamakawa, M. Hirayama, R. Kanno, M. Yonemura, T. Kamiyama, Y. Kato, S. Hama, K. Kawamoto and A. Mitsui, *Nat Mater*, 2011, 10, 682-686.

6.   R. Murugan, V. Thangadurai and W. Weppner, *Angew Chem Int Edit*, 2007, 46, 7778-7781.

7.   J. Awaka, A. Takashima, K. Kataoka, N. Kijima, Y. Idemoto and J. Akimoto, *Chem. Lett.*, 2011, 40, 60-62.

8.   S. Stramare, V. Thangadurai and W. Weppner, *Chem. Mater.*, 2003, 15, 3974-3990.

9.   J. B. Goodenough, H. Y. P. Hong and J. A. Kafalas, *Mater. Res. Bull.*, 1976, 11, 203-220.

10.   P. Knauth, *Solid State Ionics*, 2009, 180, 911-916.

11.   G. Y. Adachi, N. Imanaka and H. Aono, *Adv. Mater.*, 1996, 8, 127-135.

12.   J. M. Winand, A. Rulmont and P. Tarte, *J. Solid State Chem.*, 1991, 93, 341-349.

13.   A. Martinez-Juarez, C. Pecharroman, J. E. Iglesias and J. M. Rojo, *J. Phys. Chem. B*, 1998, 102, 372-375.

14.   E. R. Losilla, M. A. G. Aranda, M. MartinezLara and S. Bruque, *Chem. Mater.*, 1997, 9, 1678-1685.

15.   E. Morin, J. Angenault, J. C. Couturier, M. Quarton, H. He and J. Klinowski, *Eur. J. Solid State Inorg. Chem.*, 1997, 34, 947-958.

16.   H. Aono, E. Sugimoto, Y. Sadaoka, N. Imanaka and G. Adachi, *J. Electrochem. Soc.*, 1990, 137, 1023-1027.

17.   A. V. Rao, V. Veeraiah, A. V. P. Rao, B. K. Babu, B. S. Latha and K. R. Rao, *Bull. Mater. Sci.*, 2014, 37, 883-888.

18.   K. Ado, Y. Saito, T. Asai, H. Kageyama and O. Nakamura, *Solid State Ionics*, 1992, 53, 723-727.

19.   K. Arbi, W. Bucheli, R. Jimenez and J. Sanz, *J. Eur. Ceram. Soc.*, 2015, 35, 1477-1484.

20.   D. Rettenwander, A. Welzl, S. Pristat, F. Tietz, S. Taibl, G. J. Redhammer and J. Fleig, *J Mater Chem A*, 2016, 4, 1506-1513.

21.   V. Epp, Q. L. Ma, E. M. Hammer, F. Tietz and M. Wilkening, *Phys. Chem. Chem. Phys.*, 2015, 17, 32115-32121.

22.   J. Fu, *Solid State Ionics*, 1997, 96, 195-200.

23.   M. Cretin and P. Fabry, *J. Eur. Ceram. Soc.*, 1999, 19, 2931-2940.

24.   G. J. Redhammer, D. Rettenwander, S. Pristat, E. Dashjav, C. M. N. Kumar, D. Topa and F. Tietz, *Solid State Sci*, 2016, 60, 99-107.

25. A. C. T. van Duin, A. Strachan, S. Stewman, Q. S. Zhang, X. Xu and W. A. Goddard, *J. Phys. Chem. A*, 2003, 107, 3803-3811.

26. K. Chenoweth, A. C. T. van Duin, P. Persson, M. J. Cheng, J. Oxgaard and W. A. Goddard, *J. Phys. Chem. C*, 2008, 112, 14645-14654.

27. R. Fallahzadeh and N. Farhadian, *Solid State Ionics*, 2015, 280, 10-17.

28. S. Lee and S. S. Park, *Chem. Mater.*, 2012, 24, 3550-3557.

29. S. Kerisit, A. M. Chaka, T. C. Droubay and E. S. Ilton, *J. Phys. Chem. C*, 2014, 118, 24231-24239.

30. C. Tealdi, C. Spreafico and P. Mustarelli, *J. Mater. Chem.*, 2012, 22, 24870-24876.

31. T. Liang, T. R. Shan, Y. T. Cheng, B. D. Devine, M. Noordhoek, Y. Z. Li, Z. Z. Lu, S. R. Phillpot and S. B. Sinnott, *Mat Sci Eng R*, 2013, 74, 255-279.

32. F. T. Kong, H. J. Zhang, R. C. Longo, B. Lee, D. H. Yeon, J. Yoon, J. H. Park, S. G. Doo and K. Cho, *Comp Mater Sci*, 2016, 112, 193-204.

33. S. S. Berbano, J. Guo, H. Z. Guo, M. T. Lanagan and C. A. Randall, *J. Am. Ceram. Soc.*, 2017, 100, 2123-2135.

34. J. P. Maria, X. Y. Kang, R. D. Floyd, E. C. Dickey, H. Z. Guo, J. Guo, A. Baker, S. Funihashi and C. A. Randall, *J. Mater. Res.*, 2017, 32, 3205-3218.

35. J. Guo, H. Z. Guo, A. L. Baker, M. T. Lanagan, E. R. Kupp, G. L. Messing and C. A. Randall, *Angew Chem Int Edit*, 2016, 55, 11457-11461.

36. K. Chenoweth, A. C. T. van Duin and W. A. Goddard, *J. Phys. Chem. A*, 2008, 112, 1040-1053.

37. Y. K. Shin, T. R. Shan, T. Liang, M. J. Noordhoek, S. B. Sinnott, A. C. T. van Duin and S. R. Phillpot, *MRS Bull.*, 2012, 37, 504-512.

38. T. P. Senftle, S. Hong, M. M. Islam, S. B. Kylasa, Y. Zheng, Y. K. Shin, C. Junkermeier, R. Engel-Herbert, M. J. Janik, H. M. Aktulga, T. Verstraelen, A. Grama and A. C. T. van Duin, *npj Comput Mater*, 2016, 2, 15011.

39. G. Kresse and J. Furthmuller, *Phys. Rev. B: Condens. Matter*, 1996, 54, 11169-11186.

40. P. E. Blochl, *Phys. Rev. B: Condens. Matter*, 1994, 50, 17953-17979.

41. J. P. Perdew, K. Burke and M. Ernzerhof, *Phys. Rev. Lett.*, 1996, 77, 3865-3868.

42. H. J. Monkhorst and J. D. Pack, *Physical Review B*, 1976, 13, 5188-5192.

43. H. A. J. Thomas and R. Stevens, *Brit Ceram Trans J*, 1989, 88, 229-233.

44. M. E. Arroyo-DeDompablo, R. Dominko, J. M. Gallardo-Amores, L. Dupont, G. Mali, H. Ehrenberg, J. Jamnik and E. Moran, *Chem. Mater.*, 2008, 20, 5574-5584.

45. F. D. Murnaghan, *P Natl Acad Sci USA*, 1944, 30, 244-247.

46. F. Birch, *J Geophys Res*, 1952, 57, 227-286.

47. R. P. Wang, *Solid State Commun.*, 2013, 155, 88-91.

48.   W. Y. Ching and P. Rulis, *Physical Review B*, 2008, 77, 125116.

49.   J. Pellicer-Porres, A. M. Saitta, A. Polian, J. P. Itie and M. Hanfland, *Nat Mater*, 2007, 6, 698-702.

50.   R. P. Wang and M. Kanzaki, *Phys. Chem. Miner.*, 2015, 42, 15-27.

51.   A. Aatiq, M. Menetrier, L. Croguennec, E. Suard and C. Delmas, *J. Mater. Chem.*, 2002, 12, 2971-2978.

52.   B. Grabowski, T. Hickel and J. Neugebauer, *Physical Review B*, 2007, 76, 024309.

53.   A. D. Bochevarov, E. Harder, T. F. Hughes, J. R. Greenwood, D. A. Braden, D. M. Philipp, D. Rinaldo, M. D. Halls, J. Zhang and R. A. Friesner, *Int. J. Quantum Chem*, 2013, 113, 2110-2142.

54.   S. Hong and A. C. T. van Duin, *J. Phys. Chem. C*, 2015, 119, 17876-17886.

55.   S. Y. Kim, A. C. T. van Duin and J. D. Kubicki, *J. Mater. Res.*, 2013, 28, 513-520.

56.   M. V. Fedkin, Y. K. Shin, N. Dasgupta, J. Yeon, W. Zhang, D. van Duin, J. D. Kubicki, A. C. T. van Duin, K. Mori, A. Fujjiwara, M. Machida, H. Nakamura and M. Okumura, *Unpublished manuscript*.

57.   B. Narayanan, A. C. T. van Duin, B. B. Kappes, I. E. Reimanis and C. V. Ciobanu, *Modell. Simul. Mater. Sci. Eng.*, 2012, 20, 015002.

58.   C. C. W. Verlackt, E. C. Neyts, T. Jacob, D. Fantauzzi, M. Golkaram, Y. K. Shin, A. C. T. van Duin and A. Bogaerts, *New J Phys*, 2015, 17, 103005.

59.   H. Cao, B. J. Xia, Y. Zhang and N. X. Xu, *Solid State Ionics*, 2005, 176, 911-914.

60.   M. A. K. L. Dissanayake, *Ionics*, 2004, 10, 221-225.

61.   J. Guo, S. S. Berbano, H. Z. Guo, A. L. Baker, M. T. Lanagan and C. A. Randall, *Adv. Funct. Mater.*, 2016, 26, 7115-7121.

62.   A. Laio and M. Parrinello, *P Natl Acad Sci USA*, 2002, 99, 12562-12566.

63.   A. K. Tummanapelli and S. Vasudevan, *J. Phys. Chem. B*, 2014, 118, 13651-13657.

64.   A. K. Tummanapelli and S. Vasudevan, *Phys. Chem. Chem. Phys.*, 2015, 17, 6383-6388.

65.   J. M. Park, A. Laio, M. Iannuzzi and M. Parrinello, *J. Am. Chem. Soc.*, 2006, 128, 11318-11319.

66.   H. J. C. Berendsen, J. P. M. Postma, W. F. Vangunsteren, A. Dinola and J. R. Haak, *J. Chem. Phys.*, 1984, 81, 3684-3690.

67.   in *CRC Handbook of Chemistry and Physics (Internet Version 2018)*, ed. J. R. Rumble, Press/Taylor & Francis, Boca Raton, FL.

68.   K. S. Alongi and G. C. Shields, *Ann Rep Comp Chem*, 2010, 6, 113-138.

69.   B. Lang, B. Ziebarth and C. Elsasser, *Chem. Mater.*, 2015, 27, 5040-5048.

70.   M. V. Koudraichova, N. M. Harrison and S. W. de Leeuw, *Solid State Ionics*, 2003, 157, 35-38.

71. G. Nuspl, T. Takeuchi, A. Weiss, H. Kageyama, K. Yoshizawa and T. Yamabe, *J. Appl. Phys.*, 1999, 86, 5484-5491.

72. H. Aono, E. Sugimoto, Y. Sadaoka, N. Imanaka and G. Adachi, *Solid State Ionics*, 1990, 40-1, 38-42.

73. A. Rossbach, F. Tietz and S. Grieshammer, *J. Power Sources*, 2018, 391, 1-9.

74. G. B. Kunshina, O. G. Gromov, E. P. Lokshin and V. T. Kalinnikov, *Russ J Inorg Chem+*, 2014, 59, 424-430.

75. J. L. Narvaez-Semanate and A. C. M. Rodrigues, *Solid State Ionics*, 2010, 181, 1197-1204.

76. H. Aono, E. Sugimoto, Y. Sadaoka, N. Imanaka and G. Y. Adachi, *Chem. Lett.*, 1990, DOI: Doi 10.1246/Cl.1990.331, 331-334.

77. H. Morimoto, M. Hirukawa, A. Matsumoto, T. Kurahayashi, N. Ito and S. Tobishima, *Electrochemistry*, 2014, 82, 870-874.

78. M. Kotobuki, M. Koishi and Y. Kato, *Ionics*, 2013, 19, 1945-1948.

79. K. Arbi, S. Mandal, J. M. Rojo and J. Sanz, *Chem. Mater.*, 2002, 14, 1091-1097.

80. ADF2017, SCM, Theoretical Chemistry, Vrije Universiteit, Amsterdam, The Netherlands, http://www.scm.com.

81. P. A. Doyle and P. S. Turner, *Acta Crystall a-Crys*, 1968, A 24, 390-397.

82. D. T. Cromer and J. B. Mann, *Acta Crystall a-Crys*, 1968, A 24, 321-324.

83. E. C. Bucharsky, K. G. Schell, A. Hintennach and M. J. Hoffmann, *Solid State Ionics*, 2015, 274, 77-82.

FIGURES
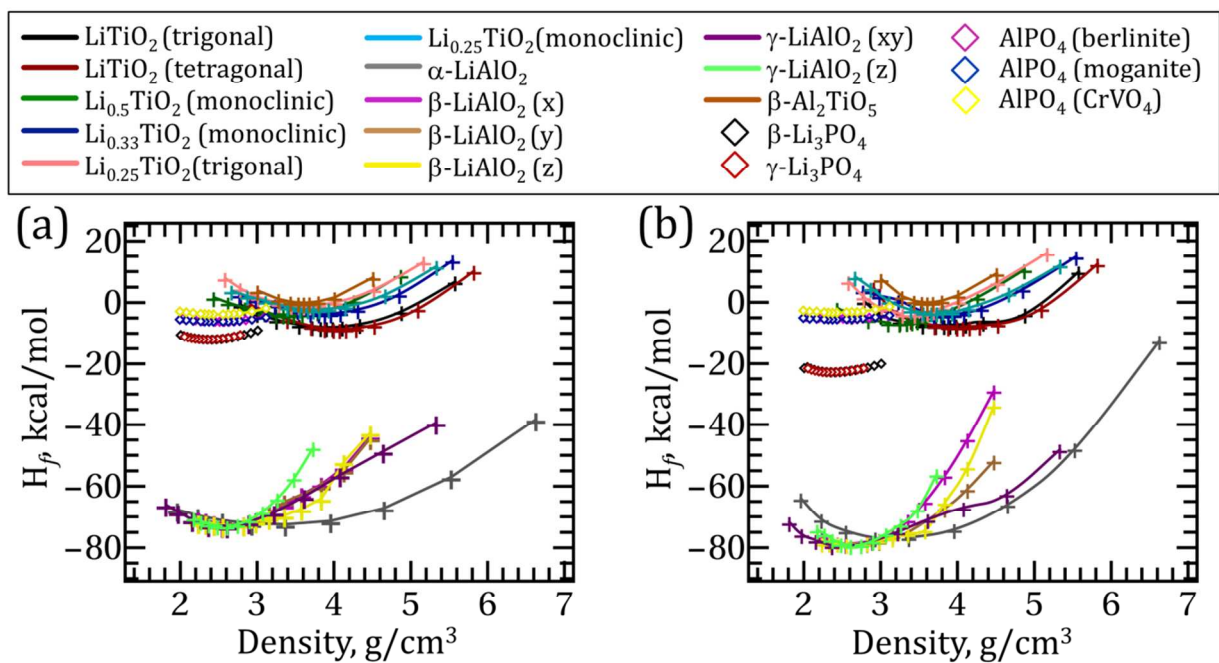
Fig. 1 Equations of state of Li$_x$TiO$_2$ (x=0.25-1.0), LiAlO$_2$ and TiAl$_2$O$_5$ oxide, and Li$_3$PO$_4$ and AlPO$_4$ phosphate crystal phases in (a) DFT and (b) ReaxFF. Heats of formation (H$_f$) per atom were calculated using bcc Li, fcc Al, molecular oxygen (O$_2$), rutile TiO$_2$, Li$_2$O, o'-P$_2$O$_5$ and α-Al$_2$O$_3$ as references at 0 K.
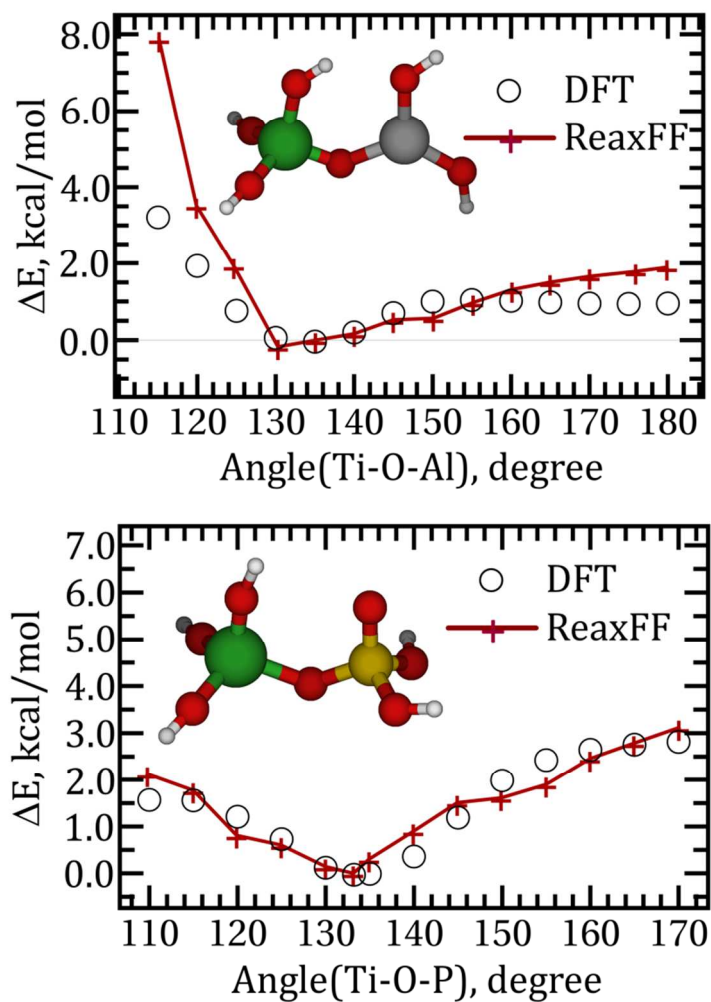
Fig. 2 Valence angle energies for Ti-O-Al (top) and Ti-O-P (bottom) bond angle in ReaxFF and DFT. Green, light gray, yellow, red and white atoms represent Ti, Al, P, O and H, respectively.
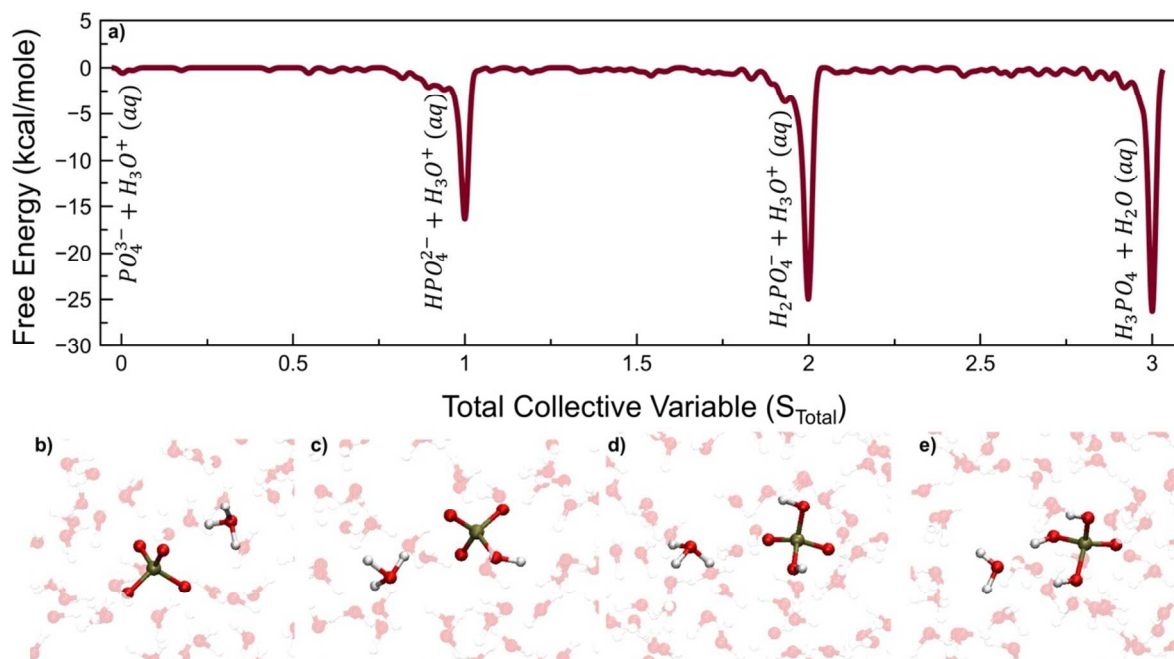
Fig. 3 (a) The free energy profile as a function of the total collective variable (S_{Total}), which is the coordination of oxygens in phosphoric acid by hydrogens. There are four peaks for dissociated and undissociated states. (b-e) The snapshots taken from the MD trajectories of metadynamics calculations. Atomic coordinates were visualized using VMD software. The phosphoric acid, hydronium ion and selected water molecules were represented differently than other molecules to increase visibility. (b) Dissociated state of HPO_4 molecule in water environment, (c) Dissociated state of H_2PO_4 molecule in water environment, d) Dissociated state of H_3PO_4 molecule in water environment, e) Undissociated state of phosphoric acid molecule in water environment.
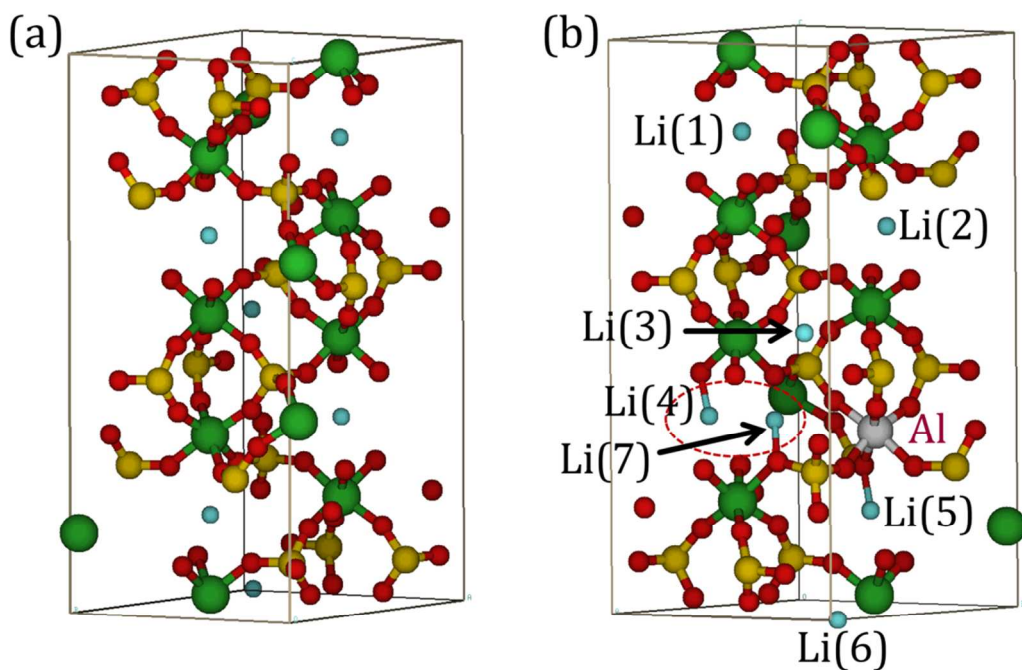
Fig. 4 Crystal structures of (a) LTP and (b) LATP (x=0.2). Li, Al, Ti, P and O atoms are colored by cyan, light gray, green, yellow and red, respectively. Li(7), which is added for charge balance in LATP, is positioned at $M_{1/2}$ site next to Al as shown in red dot circle.
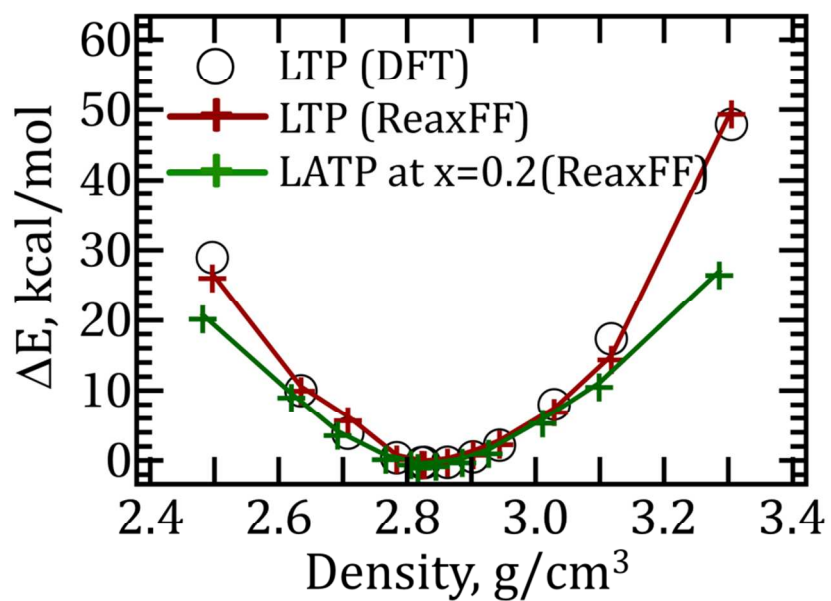
Fig. 5 Equations of state of LTP in ReaxFF and DFT and LATP (x=0.2) in ReaxFF. The LATP (x=0.2) curve shifts slightly toward the low densities (99.65% of LTP) because of the smaller lattice parameters and the lighter mass induced by the Al cation.
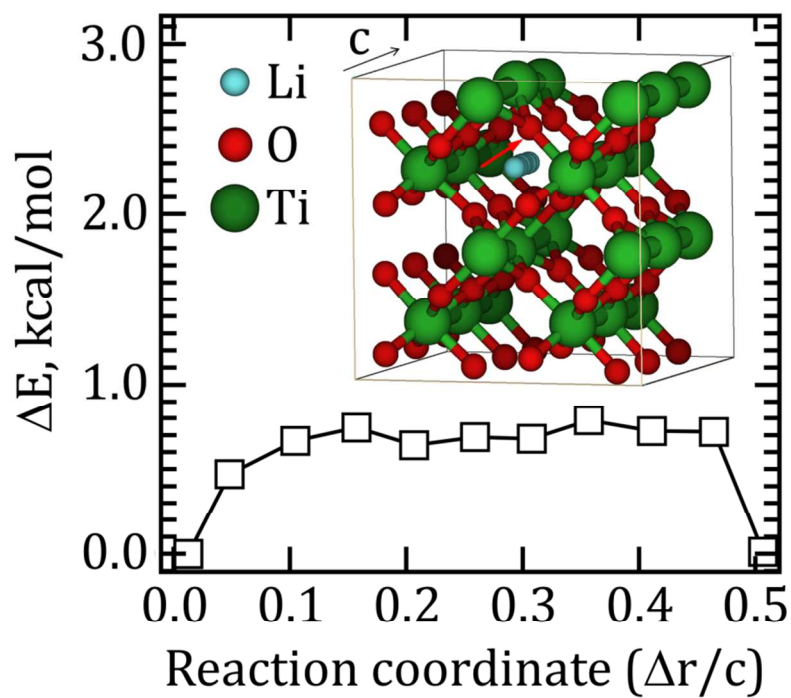
Fig. 6 Relative energy of Li diffusion in rutile TiO_2 as a function of the Li position along the diffusion pathway. The activation energy in ReaxFF is 0.8 kcal/mol, which is in good agreement with the DFT value (1.1 kcal/mol).[70] The snapshot in the graph shows the Li trajectory along the diffusion coordinate.
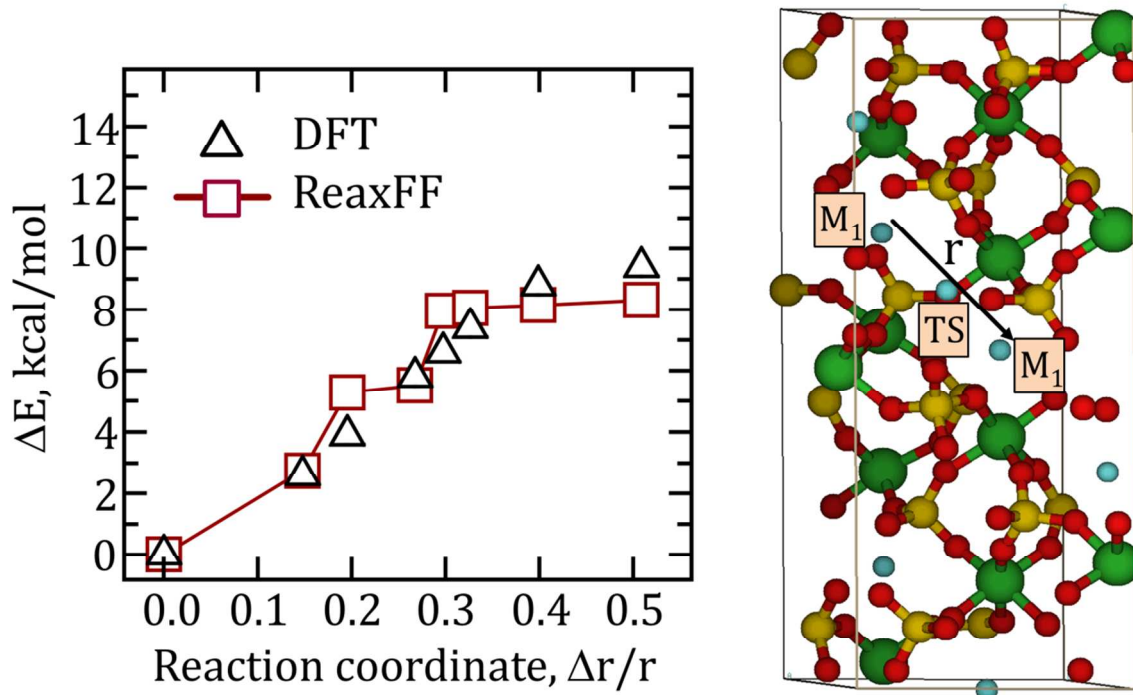
Fig. 7 Relative energy of Li diffusion via vacancy site in LTP as a function of the Li position in ReaxFF and DFT.[69] Since the M_1-to-M_1 pathway is symmetric, the potential energy profile for the half of the pathway is shown. The snapshot shows the Li position at the initial, the transition state and the final as a vacancy migrates from one M_1 site to another M_1 site. Li, Ti, P and O atoms are colored by cyan, green, yellow and red, respectively.
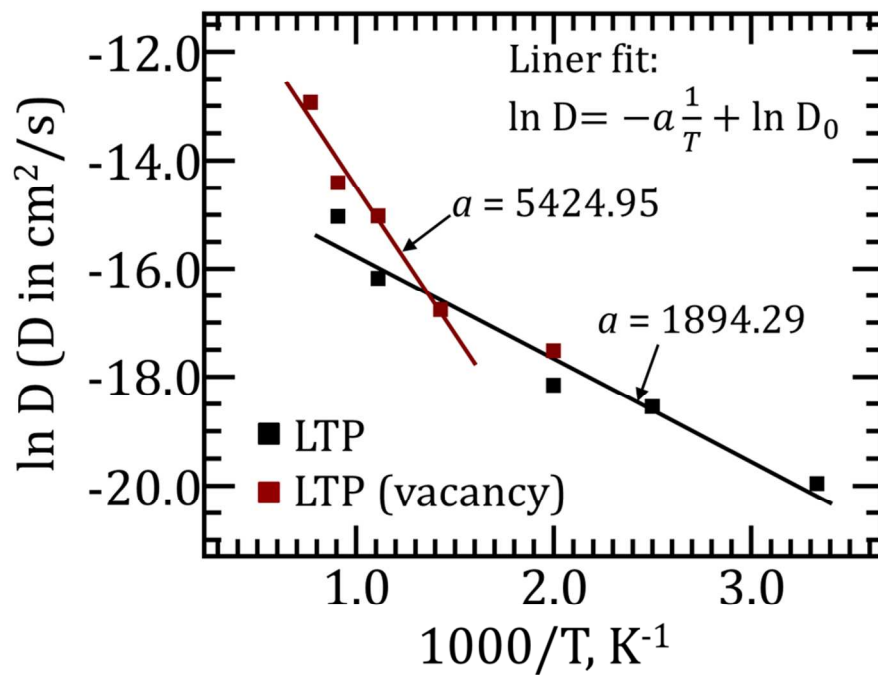
Fig. 8 Arrhenius plot, ln D vs. 1/T for Li diffusion in LTP with no vacancy and with two point vacancies per unit cell. The energy barriers for the Li diffusion are estimated to be 3.8 kcal/mol and 10.8 kcal/mol (at high temperature range), respectively.
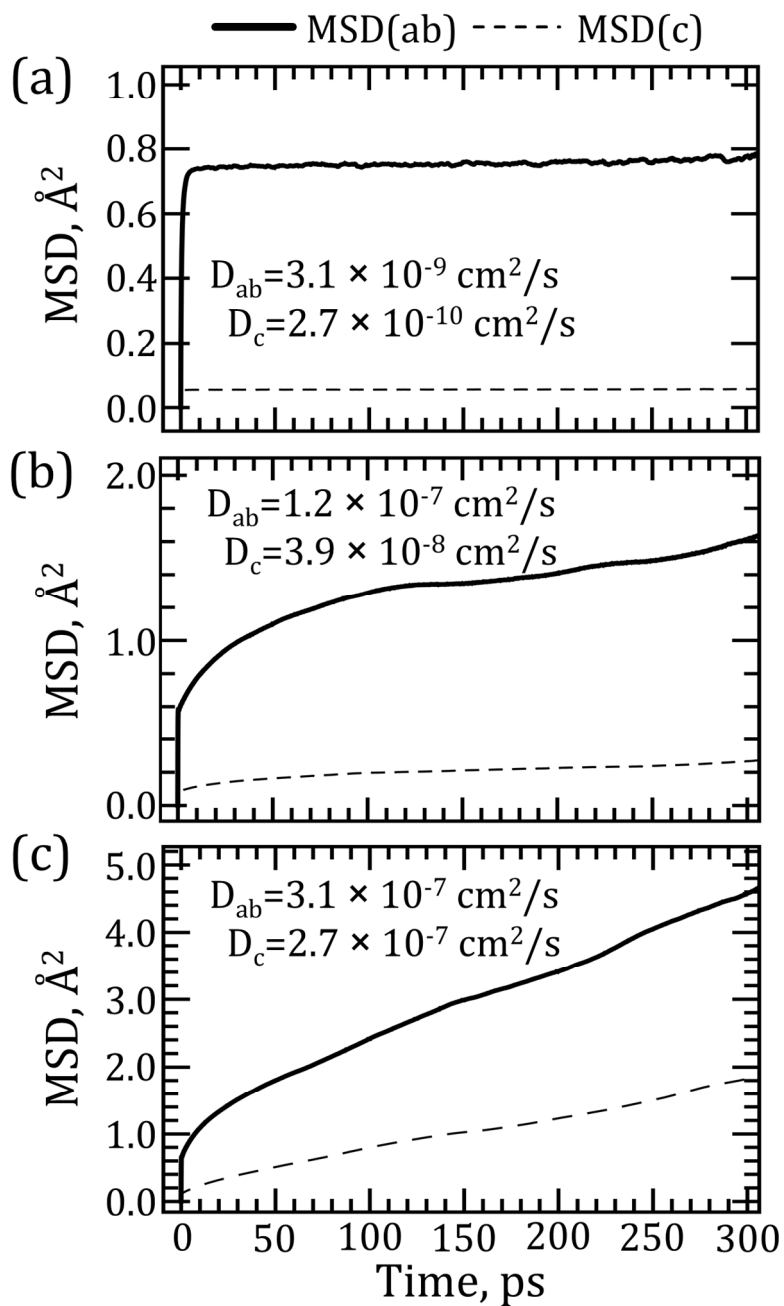
Fig. 9 Plot of the decomposed MSD(ab, c) vs. time for LTP at (a) 300 K, (b) 900 K and (c) 1100 K.

(a) LTP   (b) LATP (x=0.5)
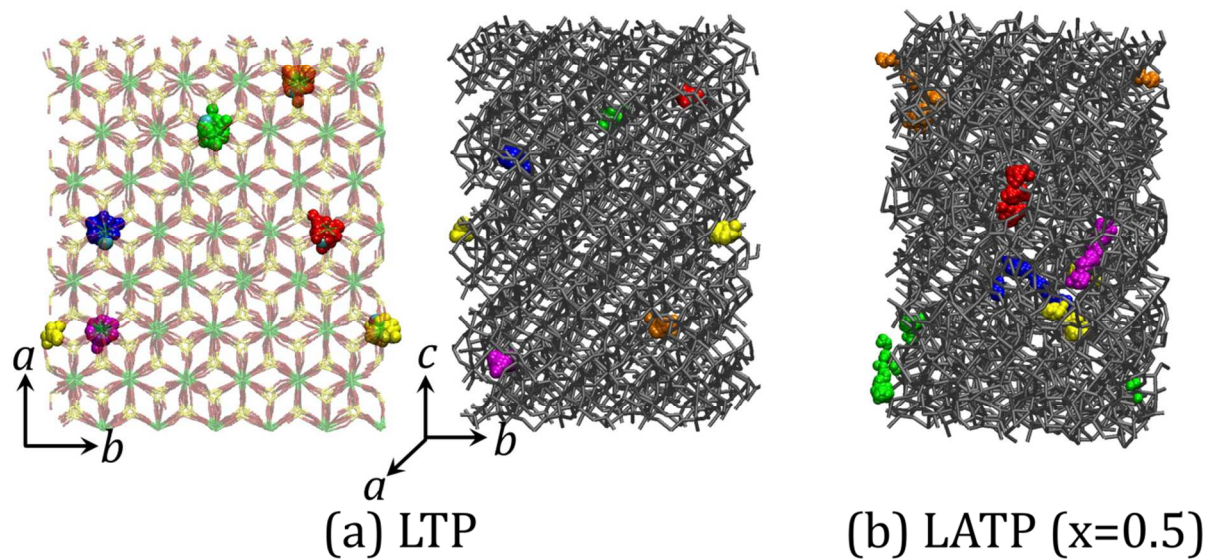
Fig. 10 Diffusion trajectories of interstitial Li atoms in LTP at 900 K (a) and LATP (x=0.5) at 1100 K (b). The trajectories of different Li atoms are distinguished by different colors. The cyan atom in the snapshot on the *ab*-plane represents Li at its initial position.
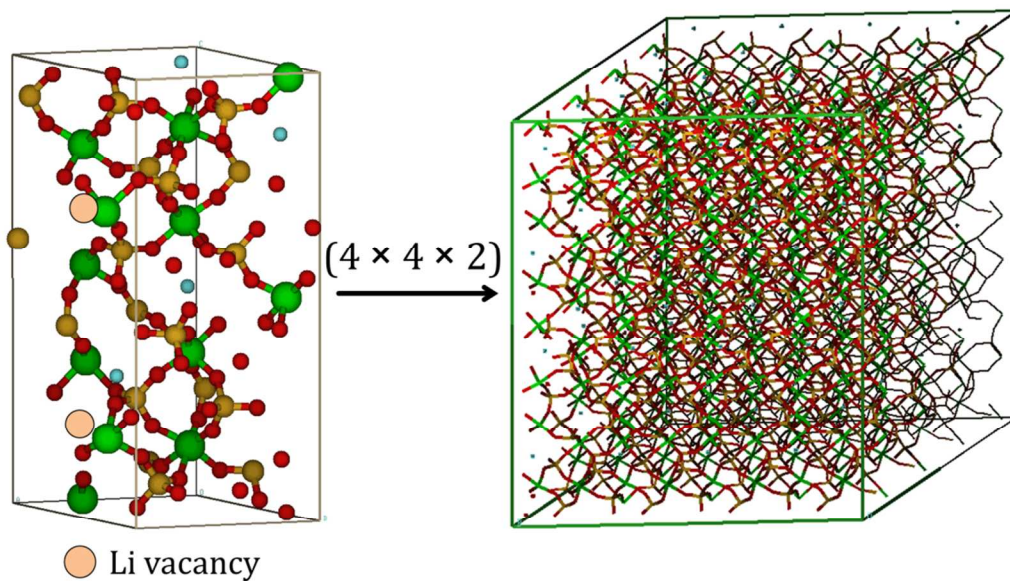
Fig. 11 A LTP unit cell with two vacancies (left) was expanded by ($4 \times 4 \times 2$) to generate a supercell for a MD simulation of Li diffusion at T = 500–1300 K. Li, Ti, P and O atoms are colored by cyan, green, yellow and red, respectively.
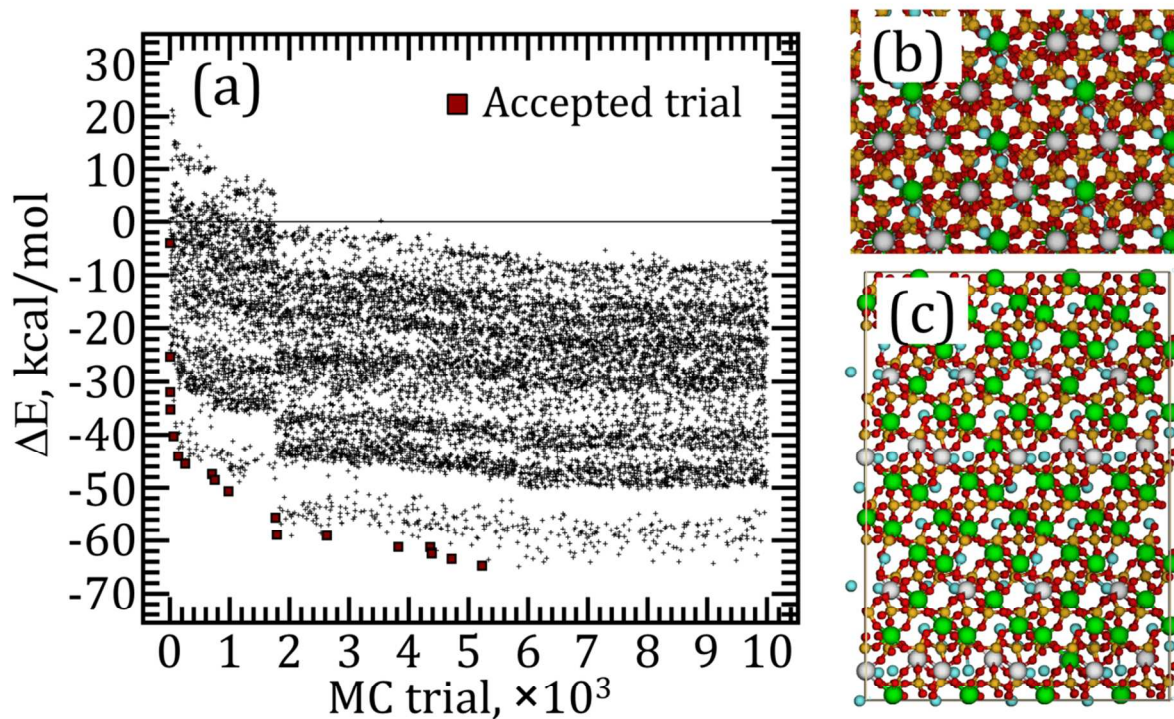
Fig. 12 A MC/MD swap (Ti ↔ Al) simulation to obtain a LATP configuration at x=0.5. (a) Potential energy of the system at MC/MD trials, (b, c) LATP final configuration (top and side view). Li, Al, Ti, P and O atoms are colored by cyan, light gray, green, yellow and red, respectively.
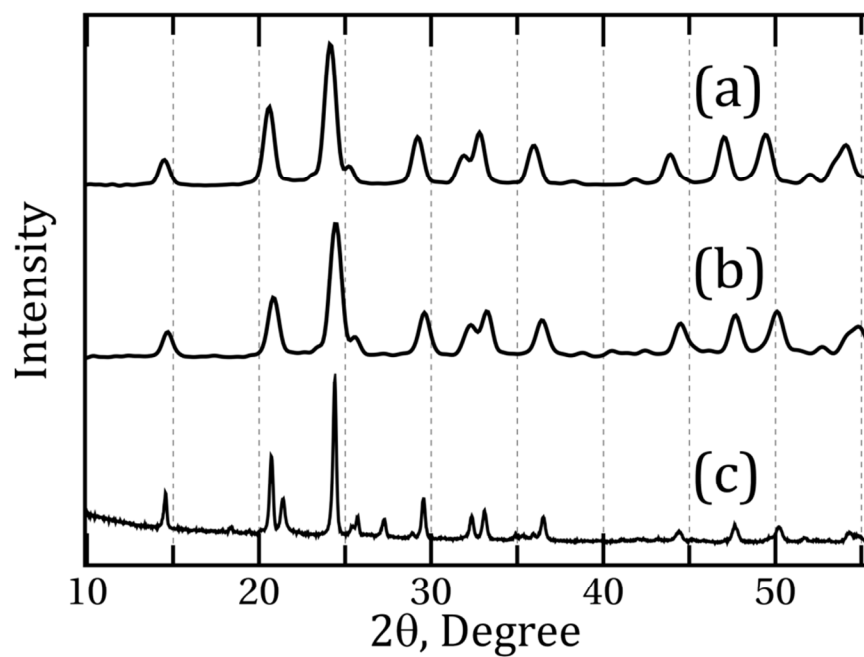
Fig. 13 X-ray diffraction patterns of (a) LTP, (b) LATP at x=0.5 taken from the MC/MD simulation in ReaxFF and (c) LATP measured from experiment.
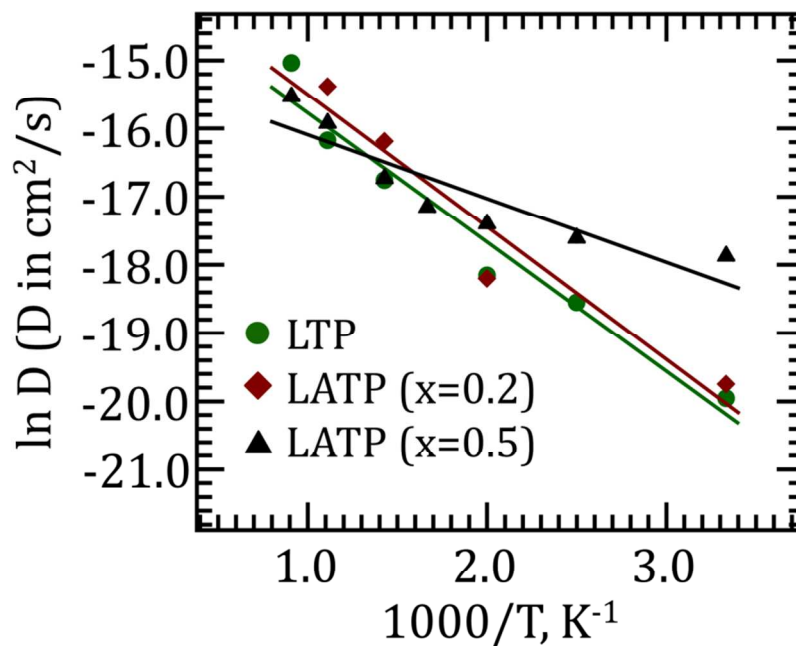
Fig. 14 Arrhenius plot, ln D vs.1/T for Li diffusion in LTP and LATP (x=0.2, 0.5). In LTP, all Li atoms are placed at M_1 site. In LATP, Li atoms are placed at either $M_{1/2}$ site or M_1 site. The energy barriers for Li diffusion are estimated to be 3.8 kcal/mol in LTP, 3.9 kcal/mol in LATP (x=0.2), and 1.9 kcal/mol in LATP (x=0.5).

Physical Chemistry Chemical Physics

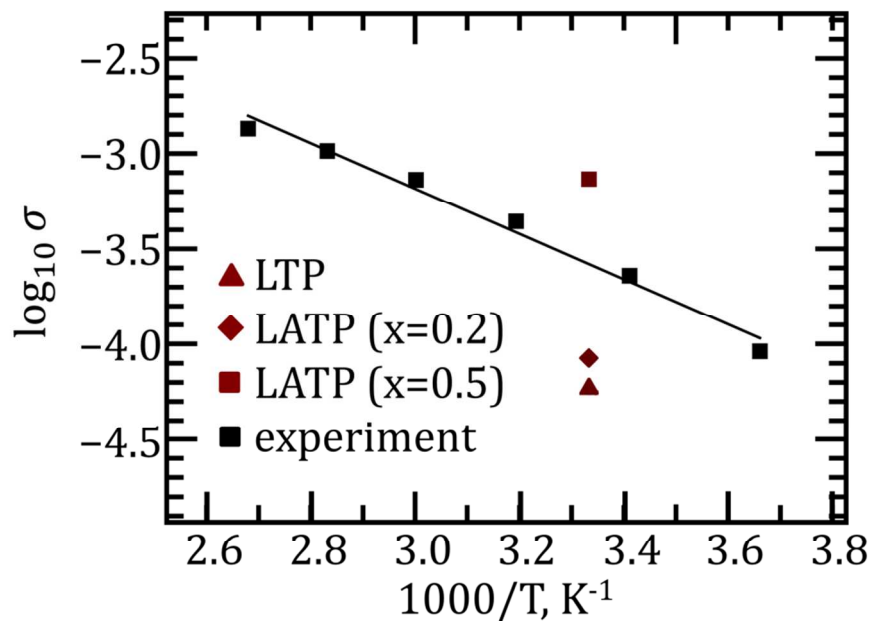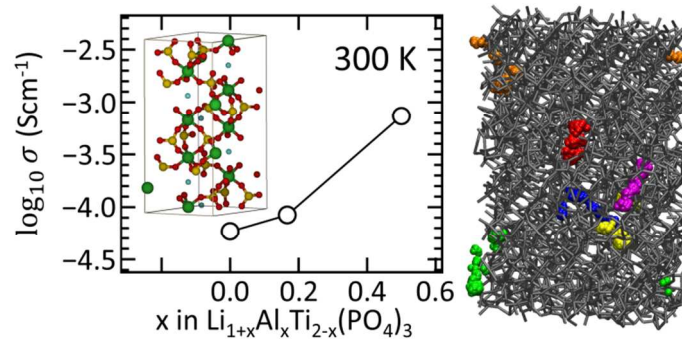Fig. 15 Plot of $\log_{10} \sigma$ vs. 1/T in LTP and LATP at x=0.2 and 0.5 in comparison with the ionic conductivity of LATP in experiment. In ReaxFF, Li ion conductivity increases from 5.9 × 10⁻⁵ S/cm (LTP) to 7.4 × 10⁻⁴ S/cm (LATP at x=0.5).

A table of contents entry

Using a ReaxFF reactive force field, we investigated the composition-dependent ionic conductivity and the Li migration behaviors in $Li_{1+x}Al_xTi_{2-x}(PO_4)_3$ solid electrolyte.